






RESEARCH ARTICLE | JANUARY 29 2024

# Effect of wall stress models and subgrid-scale models for flow past a cylinder at Reynolds number 3900 **FREE**

Guoqing Fan (范国庆) ; Yuan Liu (刘媛) ; Weiwen Zhao (赵伟文)  ; Decheng Wan (万德成) 



*Physics of Fluids* 36, 015152 (2024)

<https://doi.org/10.1063/5.0181469>



CrossMark



**APL Energy**  
**Latest Articles Online!**  
**Read Now**



# Effect of wall stress models and subgrid-scale models for flow past a cylinder at Reynolds number 3900

Cite as: Phys. Fluids **36**, 015152 (2024); doi:10.1063/5.0181469

Submitted: 16 October 2023 · Accepted: 5 January 2024 ·

Published Online: 29 January 2024



Guoqing Fan (范国庆),<sup>1</sup> Yuan Liu (刘媛),<sup>2,3</sup> Weiwen Zhao (赵伟文),<sup>1,a)</sup> and Decheng Wan (万德成)<sup>1</sup>

## AFFILIATIONS

<sup>1</sup>Computational Marine Hydrodynamics Lab (CMHL), School of Naval Architecture, Ocean and Civil Engineering, Shanghai Jiao Tong University, Shanghai 200240, China

<sup>2</sup>National Engineering Research Center of Special Equipment and Power System for Ship and Marine Engineering, Shanghai 200031, China

<sup>3</sup>Shanghai Marine Diesel Engine Research Institute, Shanghai 201108, China

<sup>a)</sup> Author to whom correspondence should be addressed: [weiwen.zhao@sjtu.edu.cn](mailto:weiwen.zhao@sjtu.edu.cn)

## ABSTRACT

The wall-modeled large eddy simulation has achieved some success in simulating wall-bounded flows. However, their predictive accuracy in separated flow still requires further validation. In this study, we employ the open-source computational fluid dynamics toolbox OpenFOAM to numerically investigate the flow past a cylinder at subcritical Reynolds numbers  $Re_D = 3900$ . At two different sampling heights,  $h = 2^{\text{nd}}$  and  $h = 4^{\text{th}}$ , three wall stress models: the algebraic model, the equilibrium wall model (EQWM), and the non-EQWM (NEQWM), and five subgrid-scale (SGS) models: the Smagorinsky (SMAG) model, the  $k$ -equation SGS (KSGS) model, the wall-adapting local eddy viscosity (WALE) model, the dynamic SMAG (DSMAG) model, and the dynamic KSGS (DKSGS) model, are selected for comparative study. Various physical quantities, including statistical flow quantities, wall pressures, time-averaged wake velocity profiles, and Reynolds stresses, are extracted and compared with the experimental data. Power spectral analyses for wake velocity are conducted, and the three-dimensional vortex structures are illustrated. The results indicate that for small sampling height, all wall models yield favorable numerical simulation results. However, for larger sampling height, the NEQWM is preferred over the other two wall models. In terms of SGS models, the DKSGS model and WALE model perform better than other SGS models. The SMAG and KSGS models, due to inherent model limitations, struggle to accurately predict the flow separation angle and the Reynolds stresses in the free shear layer.

Published under an exclusive license by AIP Publishing. <https://doi.org/10.1063/5.0181469>

## I. INTRODUCTION

Turbulence modeling, recognized as a universally challenging problem, holds great significance in enhancing the accuracy and efficiency of numerical simulations for various engineering applications. Direct numerical simulation (DNS), as a highly accurate simulation approach, directly solves the Navier–Stokes (N–S) equations on a very fine grid. Because it captures every detail in the unsteady flow fields, this renders computational cost quite substantial and it is primarily suitable for low Reynolds number basic flows. Large eddy simulation<sup>1–3</sup> (LES), as an alternative approach to DNS, focuses on resolving the large-scale structures in the flow field. For the unresolved part of the scale, LES employs subgrid-scale (SGS) models.<sup>4–7</sup> Due to its higher computational accuracy compared to Reynolds-Averaged Navier–Stokes (RANS) in predicting flow fluctuations, vortex structures, and

flow-induced noise, LES has broader prospects for applications in the engineering field.

In the academic research field, LES has become an indispensable engineering tool for predicting and analyzing unsteady, multiscale, and Multiphysics turbulent flows. In practical engineering applications, LES is not widely utilized, mainly due to the high computational demands of wall-resolved LES (WRLES) for high Reynolds number flows.<sup>8</sup> In terms of WRLES, the majority of the computational grid is dedicated to resolving the inner layer of the boundary layer flow (which occupies approximately 10%–20% of the boundary layer thickness). Chapman<sup>9</sup> presented a landmark paper in 1979 that estimated and compared the number of grid nodes  $N$  required for DNS and WRLES, emphasizing the importance of wall modeling. For a fully developed turbulent boundary layer, the size of energetic eddies in the

inner layer is on the order of the viscous length scale  $\delta_\nu = \nu/u_\tau$ . Here,  $\nu$  represents the kinematic viscosity,  $u_\tau = \sqrt{\tau_w/\rho}$  is the friction velocity on the wall, and  $\tau_w$  is the wall shear stress. The outer layer of the boundary layer is characterized by the local boundary layer thickness  $\delta$ . The ratio between them defines the Reynolds number  $Re_\tau = \delta/\delta_\nu$ , based on the friction velocity. It can be observed that as the Reynolds number increases, the energy-containing scales in the inner layer of the boundary layer decrease. Therefore, to resolve the flow in the inner layer of the boundary layer, the grid resolution needs to be of the same order as the viscous length scale, resulting in computational costs that are often impractical. As a consequence, the fundamental idea of wall-modeled LES (WMLES) is to directly compute and resolve the flow in the outer layer of the boundary layer, while using modeling approaches for the flow in the inner layer of the boundary layer. In recent years, Choi and Moin,<sup>10</sup> building on Chapman's work, reexamined the computational cost issue using more accurate formulas for high Reynolds number boundary layer flows. The study showed that the number of grid nodes of turbulent boundary layers required for DNS, WRLES, and WMLES is proportional to  $N_{DNS} \sim Re_\tau^{37/14}$ ,  $N_{WR} \sim Re_\tau^{13/7}$ , and  $N_{WM} \sim Re_L$ , where  $L$  represents the length of the flat plate. Importantly, the computational cost of WMLES exhibits a linear relationship with Reynolds number, which significantly expands the range of Reynolds numbers that WMLES can handle.

The origins of WMLES can be traced back to Schumann's research<sup>11</sup> in 1975. Schumann employed wall stress boundary conditions instead of wall velocity boundary conditions, which is commonly referred to as the wall stress model. The model that predicts the wall shear stress based on the law of the wall is typically known as the algebraic model (ALG). In terms of the law of the wall, many researchers have developed equations that satisfy the velocity distribution near the wall, such as the Werner–Wengle model<sup>12</sup> and the Spalding's law.<sup>13</sup> In addition to the ALG mentioned above, there is another approach for determining wall shear stress based on the simplified Navier–Stokes (N–S) equations in the thin boundary layer. This method involves embedding a layer of fine grids in the modeled region near the wall to solve simplified thin boundary layer equations (TBLEs); hence, it is also referred to as the two-layer model (TLM).<sup>14</sup> In this approach, LES information is sampled at the top of the embedded grids, while a no-slip velocity boundary condition is imposed at the bottom. Embedded grids are only refined in the wall-normal direction, allowing for a large aspect ratio of the grids. This approach often has advantages when dealing with non-equilibrium effects in certain flows, such as transition and separation. Based on the treatment of source terms in TBLE, TLM can be further classified into models based on ordinary differential equations (ODEs) or partial differential equations (PDEs). Among them, PDE-based models typically consider all components of source terms, including pressure gradient terms, transient terms, and convection terms. However, this approach is relatively complex, and there is no consensus on whether it provides more accurate computations.<sup>15</sup> This paper will not elaborate on PDE-based models in detail. In addition, ODE-based models simplify the source terms. One approach is to directly set the source term to zero, which is commonly known as the equilibrium ODE-based wall model (EQWM). Another approach is to consider only the pressure gradient term in the source term, known as the non-equilibrium ODE-based wall model (NEQWM). This approach has attracted significant attention in separated flows with adverse pressure gradients.

Currently, many scholars<sup>16–20</sup> have numerically simulated various flow phenomena at different Reynolds numbers using wall stress models. For channel flow with zero adverse pressure gradient, the simple ALG has been demonstrated to accurately predict time-averaged quantities<sup>16</sup> such as velocity profiles and time-averaged Reynolds stresses for fully developed turbulence. However, for separated flows with strong adverse pressure gradients, the law of the wall will no longer exist.<sup>21</sup> In such cases, the TLM approach is usually considered, as it provides accurate wall shear stress based on TBLE. In terms of the source term in TBLE, Larsson *et al.*<sup>15</sup> pointed out that flow regions with strong adverse pressure gradients often correspond to areas with large convective terms, and their effects can balance each other. Additionally, WMLES only models the inner layer of the boundary layer, while the non-equilibrium effects of the outer layer can be well captured by LES. Therefore, the EQWM can still be used for separated flows with strong adverse pressure gradients. In this regard, Iyer and Malik<sup>22</sup> numerically simulated the flow past a wall-mounted hump using the EQWM and compared the numerical results obtained from different sampling heights,  $h = 1^{\text{st}}$  and  $h = 3^{\text{rd}}$  ( $h = n^{\text{th}}$  represents sampling at the  $n^{\text{th}}$  cell center in the wall-normal direction). The results validated the reliability of this approach, and they obtained better predictions of the time-average velocity and stress in the separation region when sampling height set  $h = 3^{\text{rd}}$ . Ren *et al.*<sup>23</sup> numerically simulated three typical separated flows using the EQWM and detached eddy simulation (DES). The sampling heights was set  $h = 3^{\text{rd}}$ . The results showed that both methods accurately predicted the separation location and wake characteristics, but simulating flow separation requires a more refined grid. Duprat *et al.*,<sup>24</sup> considering the non-equilibrium effects of the pressure gradient, numerically simulated periodic hill flows and obtained good numerical results in the flow separation region. Wang and Moin<sup>25</sup> compared the predictive accuracy of the EQWM and the NEQWM in predicting flow separation at the trailing edge of an airfoil. The results showed that the NEQWM provided a better qualitative prediction of the wall friction coefficient. More recently, Chen *et al.*<sup>26</sup> studied SUBOFF-related flows at high Reynolds numbers using the EQWM and the NEQWM. They systematically analyzed the effects of wall models and sampling height on the time-averaged numerical simulation results. The results showed that the NEQWM performed better in predicting the surface shear stress of the hull compared to the EQWM. Additionally, the best numerical simulation results were obtained when the sampling height was set at  $y/\delta = 0.05$ . However, some papers have indicated that considering the pressure gradient term alone does not yield satisfactory results. Catalano *et al.*,<sup>27</sup> considering the non-equilibrium effects of the pressure gradient in flow past a cylinder, overpredicted the wall friction on the front of the cylinder.

In general, the prediction errors of WMLES primarily originate from two aspects. One is the modeling errors of the wall model. The accuracy of the ALG in predicting separated flows still needs further verification, and the correct treatment of source term in ODE-based wall models remains an open problem. Another is the modeling errors related to the subgrid scale. The computational results from different SGS models often exhibit differences, especially in the case of near-wall flow and separated flow. The three-dimensional flow past a cylinder at a subcritical Reynolds number  $Re_D = 3900$  serves as a classic case for separated flow. Numerous researchers<sup>28–31</sup> have conducted physical experiments on the flow past a cylinder at this Reynolds number,

providing abundant experimental data for comparison. Many scholars<sup>31–34</sup> have used this case to validate newly developed turbulent numerical simulation methods. Ren *et al.*<sup>23</sup> compared numerical simulation results of the EQWM and detached-eddy simulation for flow past a cylinder at  $Re_D = 3900$ . However, they only considered one sampling height, and they did not provide a detailed comparison of the computational differences between the EQWM and the NEQWM. In terms of SGS models, they only presented results for different SGS models in terms of surface pressure distribution, without further analysis of flow separation and wake characteristics. Therefore, in the present study, we numerically simulate the flow past a cylinder at Reynolds number  $Re_D = 3900$  using the open-source computational fluid dynamics platform OpenFOAM. Three wall modeling approaches, namely, the ALG, the EQWM, and the NEQWM, are systematically compared in terms of their predictive accuracy for separated flows at different sampling heights,  $h = 2^{\text{nd}}$  and  $h = 4^{\text{th}}$ . In addition, the effect of different SGS models will be validated in this paper. We systematically compare five SGS models, including the Smagorinsky (SMAG) model,<sup>1</sup> the  $k$ -equation SGS (KSGS) model,<sup>6</sup> the wall-adapting local eddy viscosity (WALE) model,<sup>5</sup> the dynamic Smagorinsky (DSMAG) model,<sup>3,4</sup> and the dynamic  $k$ -equation SGS (DKSGS) model,<sup>7</sup> in combination with wall stress models to assess their predictive accuracy for separated flows. These five SGS models encompass algebraic eddy viscosity models, one-equation SGS models, static SGS models in which the model coefficients are constant and dynamic SGS models. The aim is to provide a comprehensive assessment of various types of SGS models.

The paper is organized as follows: In Sec. II, we introduce the SGS models, wall models, computational domain, mesh, and numerical schemes. In Sec. III, we compare the numerical simulation performance of the three wall stress models at two different sampling heights and the effect of different SGS models. The final conclusions are drawn in Sec. IV.

## II. NUMERICAL METHODOLOGY

### A. Governing equations

LES is incapable of resolving vortices of all scales in the flow field. By applying a filter to the incompressible N–S equations,<sup>35</sup> the governing equations for LES can be obtained as

$$\frac{\partial \tilde{u}_i}{\partial t} + \frac{\partial \tilde{u}_i \tilde{u}_j}{\partial x_j} = -\frac{1}{\rho} \frac{\partial \tilde{p}}{\partial x_i} + \nu \frac{\partial^2 \tilde{u}_i}{\partial x_j \partial x_j} - \frac{\partial \tau_{ij}}{\partial x_j}, \quad (1)$$

$$\frac{\partial \tilde{u}_i}{\partial x_i} = 0, \quad (2)$$

where  $\tilde{u}_i$  ( $i = 1, 2, \text{ and } 3$ ) is the filtered velocity component in the  $x_i$  direction of the flow field,  $\tilde{p}$  is the filtered pressure of the flow field,  $\nu$  is the kinematic viscosity of the fluid, and  $\tau_{ij}$  is the SGS stress term.  $\tau_{ij}$  is given by

$$\tau_{ij} = \frac{2}{3} k_{\text{sgs}} \delta_{ij} - 2\nu_{\text{sgs}} \tilde{S}_{ij}, \quad (3)$$

where  $k_{\text{sgs}}$  is the SGS kinetic energy,  $\tilde{S}_{ij}$  is the resolved strain-rate tensor,  $\delta_{ij}$  is the Kronecker delta, and  $\nu_{\text{sgs}}$  is the SGS eddy viscosity. Once  $\nu_{\text{sgs}}$  is determined,  $\tau_{ij}$  can be obtained, and Eq. (1) can be closed.

Five classical SGS models and three wall models are used in this study. The details of them are given in Appendixes A and B.

### B. Numerical settings

#### 1. Computational domain, boundary condition, and mesh

The computational domain and mesh are described below. Taking the cylinder center as the origin, the  $x$  axis represents the incoming flow direction, the  $y$  axis is perpendicular to the incoming flow direction, and the  $z$  axis corresponds to the axial direction of the cylinder. The computational domain, as shown in Fig. 1, extends to  $-15D < x < 30D$ ,  $-15D < y < 15D$ , and  $-\pi D/2 < z < \pi D/2$ , in which  $D = 0.01$  m is the diameter of the cylinder.

As for the boundary conditions, the inlet is set as a uniform inflow with a velocity of 0.39 m/s and zero-gradient pressure condition. The outlet has a zero-gradient velocity condition, and the pressure condition is set as 0. The cylinder employs a no-slip velocity boundary condition and a zero-gradient pressure condition. The remaining boundaries are set as symmetry boundaries.

Figure 2 shows the overall and local schematics of the computation mesh. Within the range of  $r = 7D$  around the cylinder, an O-type mesh is implemented. The O-type mesh comprises a total of 100 cell numbers in the radial direction and 200 cell numbers in the circumferential direction, while the axial direction of the cylinder employs 30 cell numbers. The height of the first layer of mesh cells normal to the wall is  $\Delta_{||,1} \approx 5 \times 10^{-3} D$ , which is larger than  $1 \times 10^{-4} D$  used by Jiang and Cheng<sup>36</sup> and  $3.5 \times 10^{-3} D$  used by Franke and Frank.<sup>37</sup> Hence, we adopted a wall modeling approach. In actual calculations,  $y^+$  slightly exceeds 1, resulting in a final mesh volume of approximately 849 000. The non-dimensional time step  $\Delta t^* = \Delta t U_\infty / D$  is set as 0.039. The convergence analysis of mesh and time step will be further investigated in Sec. II C.

#### 2. Numerical schemes

In terms of the discretization scheme for the convective term, given the relatively coarse grid near the wall in WMLES, employing the common linear interpolation scheme used in WRLES could potentially introduce numerical oscillations. The use of the upwind scheme will introduce additional numerical dissipation, but it provides relatively better computational stability. In the present study, all numerical simulations adopt the linear upwind stabilized transport (LUST) scheme.<sup>38,39</sup> This scheme uses a weighted average of 75% linear central and 25% linear upwind scheme to compute cell-face values, resulting

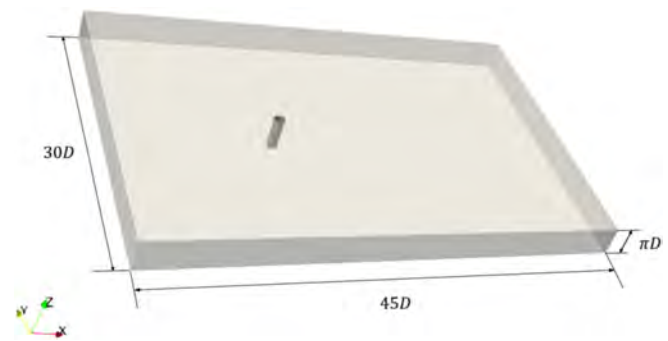


FIG. 1. Computational domain.

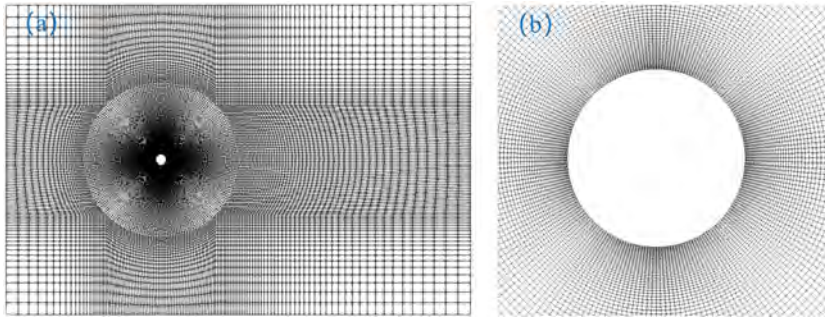


FIG. 2. Computational mesh in (a) global view on the x-y plane and (b) local view.

TABLE I. Computational cases for convergence study.

Case	$N_\theta$	$N_r$	$N_z$	$N_{\text{Total}}$	$\Delta t^*$
1	200	100	30	849 000	$3.9 \times 10^{-2}$
2	200	100	30	849 000	$7.8 \times 10^{-2}$
3	200	100	30	849 000	$1.95 \times 10^{-2}$
4	160	80	24	480 000	$3.9 \times 10^{-2}$
5	240	120	36	1 380 000	$3.9 \times 10^{-2}$

in second-order accuracy. In addition, the temporal terms employ a second-order implicit backward difference method,<sup>40</sup> while the diffusion term is discretized using the Gaussian linear conservation scheme. The coupled pressure-velocity is solved using the PIMPLE algorithm, with two pressure corrections in each time step.

### C. Convergence study of mesh and time step

In order to evaluate the convergence of the current computational mesh and time step, we conduct the convergence study using different meshes and time steps. The specific mesh distributions and time step selections are shown in Table I. Here,  $N_\theta$ ,  $N_r$ , and  $N_z$  represent the

number of cells in the circumferential, radial, and axial directions, respectively, with  $N_{\text{Total}}$  indicating the total cell count. Cases 1 to 3 employ the same computational mesh with varying time steps, primarily aimed at assessing whether the current computational time steps meet the computational requirements. Cases 1, 4, and 5 use identical time steps but different computational meshes, serving to verify whether the present meshes satisfy the computational requisites. All cases are preliminarily using the WALE model and NEQWM, with a sampling height of  $h = 4^{\text{th}}$ .

Table II presents the statistical flow quantities of flow past the cylinder. These quantities include the time-averaged drag coefficient  $\bar{C}_d$ , root mean square of the lift coefficient  $(C_l)_{\text{rms}}$ , time-averaged pressure coefficient  $\bar{C}_{pb}$  at stagnation point behind the cylinder, the relative recirculation length  $L_{\text{rec}}/D$ , flow separation angle  $\theta_{\text{sep}}$ , and Strouhal number ( $St$ ). The lift and drag coefficients are defined as

$$C_l = \frac{F_l}{\frac{1}{2} \rho U_\infty^2 A}, \quad (4)$$

$$C_d = \frac{F_d}{\frac{1}{2} \rho U_\infty^2 A}, \quad (5)$$

where  $F_d$  and  $F_l$  are the forces acting on the cylinder in the  $x$  and  $y$  directions, respectively.  $A$  is the frontal area of the cylinder, and  $U_\infty$

TABLE II. Statistical flow quantities for flow past a cylinder.

Data from	$\bar{C}_d$	$(C_l)_{\text{rms}}$	$-\bar{C}_{pb}$	$L_{\text{rec}}/D$	$\theta_{\text{sep}}$ (deg)	$St$
Lourenco <sup>28</sup> (Exp)	0.99	...	...	1.19	86	0.22
Norberg <sup>29</sup> (Exp)	0.98	0.04–0.15	0.90	...	...	...
Parnaudeau <i>et al.</i> <sup>31</sup> (Exp)	...	...	...	1.51	88	0.208
Ma <i>et al.</i> <sup>41</sup> (DNS)	...	...	0.84	1.59	88	0.219
Tian and Xiao <sup>42</sup> (LES)	0.98	...	0.85	1.64	88	...
Ren <i>et al.</i> <sup>23</sup> (WMLES)	1.000	0.104	0.824	1.662	88.81	0.209
Case1	1.020	0.149	0.908	1.519	85.914	0.207
Case2	0.993	0.102	0.856	1.671	85.428	0.201
Case3	1.007	0.134	0.901	1.557	87.633	0.207
Case4	1.122	0.302	1.057	1.150	86.794	0.202
Case5	0.994	0.116	0.881	1.629	85.293°	0.209

denotes the inflow velocity. The formula for the surface pressure coefficient is given by

$$C_p = \frac{p - p_0}{\frac{1}{2}\rho U_\infty^2}, \quad (6)$$

where  $p$  is the pressure on the surface of the cylinder and  $p_0$  is the reference pressure at the outlet boundary.  $St$  is defined as

$$St = \frac{fD}{U_\infty}, \quad (7)$$

where  $D$  is the diameter of the cylinder and  $f$  is the shedding frequency of vortices.

From Table II, it can be observed that, except for case 4, the errors in the computational results compared to experimental and other numerical simulation data fall within reasonable ranges. Case 4, conducted on a coarser grid, exhibits a shorter length of the recirculation zone in the numerical simulations. The shorter length of the recirculation zone corresponds to higher lift and drag coefficients, consistent with the results from previous literature.<sup>43,44</sup> Moreover, simulation conducted on fine grids results in a slightly longer recirculation zone compared to that on middle grids. This primarily stems from the refinement of the axial grid, leading to a slight overestimation of the recirculation zone length, aligning with earlier reports.<sup>36,45,46</sup>

Figure 3 shows the time-averaged pressure coefficients on the surface of the cylinder. Similarly, case 4, simulated on a coarse grid, exhibits a significant deviation from the experimental data, while the results for other cases agree well with the experimental data. This strongly affirms that the computational mesh and time step utilized in case 1 meet the computational requirements. Consequently, all subsequent numerical simulations will be based on the mesh and computational time step settings established in case 1.

### III. RESULTS AND DISCUSSION

In this section, we compare the accuracy of three different wall models and the combination of different SGS models with wall stress models. The computational cases are outlined in Table III. For cases 1–6, we compare the accuracy of three different wall models, namely, the ALG, the EQWM, and the NEQWM. The SGS model used in cases

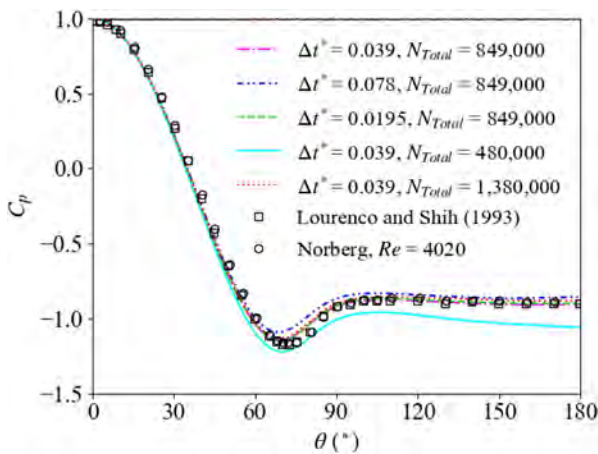


FIG. 3. Time-averaged pressure distribution on the cylinder surface.

TABLE III. Computational cases.

Case	Wall model	SGS model	$h$	$\Delta h/D$
1	ALG	WALE	2 <sup>nd</sup>	$7.62 \times 10^{-3}$
2	EQWM	WALE	2 <sup>nd</sup>	$7.62 \times 10^{-3}$
3	NEQWM	WALE	2 <sup>nd</sup>	$7.62 \times 10^{-3}$
4	ALG	WALE	4 <sup>th</sup>	$1.86 \times 10^{-2}$
5	EQWM	WALE	4 <sup>th</sup>	$1.86 \times 10^{-2}$
6	NEQWM	WALE	4 <sup>th</sup>	$1.86 \times 10^{-2}$
7	NEQWM	SMAG	4 <sup>th</sup>	$1.86 \times 10^{-2}$
8	NEQWM	KSGS	4 <sup>th</sup>	$1.86 \times 10^{-2}$
9	NEQWM	DSMAG	4 <sup>th</sup>	$1.86 \times 10^{-2}$
10	NEQWM	DKSGS	4 <sup>th</sup>	$1.86 \times 10^{-2}$

1–6 is the WALE model. Due to the potential variations in results for different wall models at different sampling heights, and since sampling in the first cell off the wall will introduce computational errors,<sup>16,22</sup> we choose two sampling heights:  $h = 2^{\text{nd}}$  and  $h = 4^{\text{th}}$ . The wall-normal distances from the sampling points to the wall are  $\Delta h \approx 7.62 \times 10^{-3}D$  and  $\Delta h \approx 1.86 \times 10^{-2}D$ , respectively. For cases 7–10, we consider four SGS models other than WALE, namely, the SMAG model, the KSGS model, the DSMAG model, and the DKSGS model. The wall model and sampling height are NEQWM and  $h = 4^{\text{th}}$ , respectively.

Franke and Frank<sup>37</sup> suggested that at least 40 shedding cycles are required to achieve converged time-averaged results. In the previous study by Parnaudeau *et al.*,<sup>31</sup> 60 shedding cycles of temporal data were used. In the present study, each case was simulated for 780 dimensionless time units, where the initial 78 dimensionless time units were used for flow development, leaving 702 dimensionless time units for characterizing the flow. The statistical time span covers at least 175 shedding cycles.

#### A. Effect of wall stress models

For the flow past a cylinder at subcritical Reynolds number  $Re_D = 3900$ , the boundary layer is in a laminar state before flow separation, and a periodic shedding of Karman vortex street is formed in the wake region after flow separation. Table IV presents the statistical flow quantities for the flow past the cylinder using three different wall models.

From Table IV, it can be observed that when the sampling height is set as  $h = 2^{\text{nd}}$ , the ALG yields a longer recirculation length and an earlier separation location. Parnaudeau *et al.*<sup>31</sup> pointed out that the agreement of the recirculation length with experimental results is the most significant indicator of numerical simulation accuracy. In terms of predicting the recirculation length, the EQWM exhibits the best agreement with the experimental data, but it predicts a relatively smaller  $\theta_{\text{sep}}$ . The  $L_{\text{rec}}/D$  predicted by NEQWM differs from the experiment by only 2%, yet it offers a more accurate prediction of the location of flow separation. Figure 4 shows the time-averaged wall-normal velocity gradient for the three wall models at the smaller sampling height. The location where the velocity gradient transitions from positive to negative corresponds to the occurrence of flow separation.

The results of  $h = 4^{\text{th}}$  in Table IV indicate that when the sampling height is set relatively larger, significant differences exist in the

TABLE IV. Statistical flow quantities for flow past a cylinder.

Data from	$\bar{C}_d$	$(C_l)_{rms}$	$-\bar{C}_{pb}$	$L_{rec}/D$	$\theta_{sep}$ (deg)	$St$
Lourenco <sup>28</sup> (Exp)	0.99	...	...	1.19	86	0.22
Norberg <sup>29</sup> (Exp)	0.98	0.04–0.15	0.90	...	...	...
Parnaudeau <i>et al.</i> <sup>31</sup> (Exp)	...	...	...	1.51	88	0.208
Ma <i>et al.</i> <sup>41</sup> (DNS)	...	...	0.84	1.59	88	0.219
Tian and Xiao <sup>42</sup> (LES)	0.98	...	0.85	1.64	88	...
Ren <i>et al.</i> <sup>23</sup> (WMLES)	1.000	0.104	0.824	1.662	88.81	0.209
ALG, WALE, $h = 2^{nd}$	1.010	0.123	0.891	1.638	85.261	0.204
EQWM, WALE, $h = 2^{nd}$	1.035	0.165	0.914	1.514	85.365	0.202
NEQWM, WALE, $h = 2^{nd}$	1.010	0.142	0.902	1.549	87.405	0.205
ALG, WALE, $h = 4^{th}$	1.112	0.224	1.015	1.287	85.117	0.199
EQWM, WALE, $h = 4^{th}$	1.078	0.179	0.961	1.436	84.850	0.198
NEQWM, WALE, $h = 4^{th}$	1.020	0.149	0.908	1.519	85.914	0.207

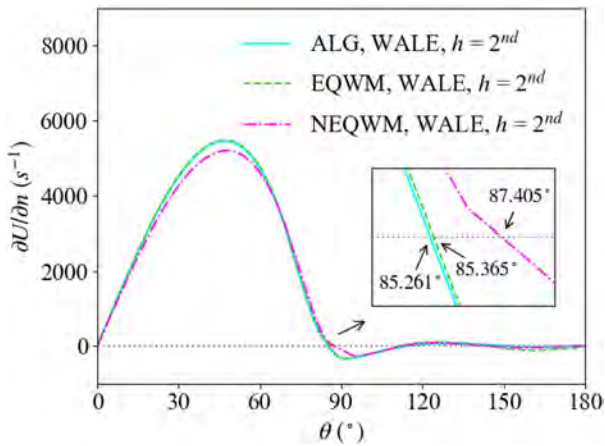


FIG. 4. Wall-normal velocity gradients predicted by the three wall models when  $h = 2^{nd}$ .

predictions among different wall models. The NEQWM yields the best results, showing an excellent agreement with the experimental data overall. On the other hand, the ALG and EQWM produce relatively larger values for  $\bar{C}_d$ . The main reason for this is that these two wall models overestimate the negative pressure at the rear of the cylinder, leading to a significant pressure difference before and after the cylinder. Additionally, the flow velocity decreases rapidly behind the cylinder, resulting in a relatively shorter length of the recirculation region. Compared to the experimental data, the ALG and EQWM underestimated the values of  $L_{rec}/D$  by 14.8% and 5%, respectively.

Figure 5 shows the surface pressure coefficients predicted by three wall models, which are compared with the experimental data from Lourenco<sup>28</sup> and Norberg.<sup>29</sup> The stagnation point is at  $0^\circ$ , and the rear of the cylinder is at  $180^\circ$ . From the comparison, it can be observed that all three wall models provide satisfactory results at a smaller sampling height,  $h = 2^{nd}$ . Prior to flow separation, the boundary layer is in a laminar state, the flow is under favorable pressure gradient, and all three wall models predict the pressure coefficient accurately in this region. However, within the range of  $60^\circ$ – $90^\circ$  where flow separation

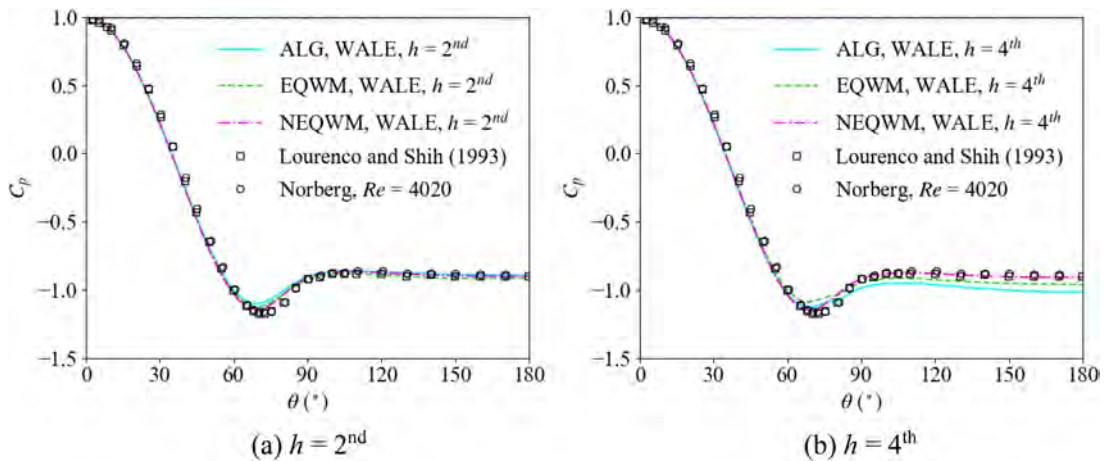


FIG. 5. Time-averaged pressure distribution on the cylinder surface.

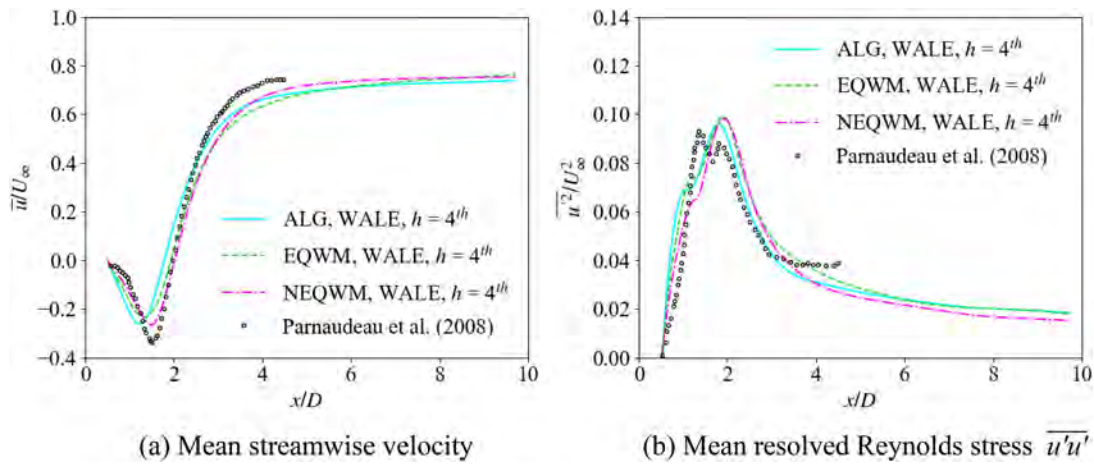


FIG. 6. (a) Mean streamwise velocity and (b) mean resolved Reynolds stress along wake centerline when  $h = 4^{th}$ .

occurs, the result from NEQWM agrees better with the experimental data. The results from ALG and EQWM are slightly higher than the experimental data overall. At a larger sampling height,  $h = 4^{th}$ , discrepancies arise among the three wall models, particularly in the surface pressure at the rear of the cylinder. The ALG and EQWM overestimate the surface negative pressure at the rear by 12.8% and 6.8%, respectively. In contrast, the NEQWM continues to exhibit good agreement with the experimental data.

Figure 6 shows the streamwise velocity and Reynolds stress profiles along the wake centerline, predicted by the three wall models at a larger sampling height,  $h = 4^{th}$ , in comparison with particle image velocimetry (PIV) experimental data from Parnaudeau.<sup>31</sup> From Fig. 6(a), we can get a clearer view of the recirculation region length predicted by the three wall models, with the NEQWM showing better agreement with the experimental data. Figure 6(b) shows the Reynolds stress normalized with  $U_{\infty}^2$ . The experimental data display two peaks before gradually decaying to zero. In contrast, the numerical simulation results exhibit a slight step at the first peak, aligning with many LES outcomes.<sup>31,47</sup>

Figure 7 shows the comparison of velocity and pressure contours between the ALG and NEQWM at a larger sampling height,  $h = 4^{th}$ . The velocity contour depicts non-dimensionalized time-averaged streamwise velocity, divided by the incoming flow velocity. The pressure contour is represented by the coefficient of pressure  $C_p$ . From the velocity contour, it is evident that the ALG predicts a shorter recirculation length at  $h = 4^{th}$ , corresponding to the data presented in Fig. 6(a). Additionally, the pressure contour indicates that the ALG yields lower pressure coefficients at the rear of the cylinder, consistent with the data shown in Fig. 5(b). In the region of laminar flow prior to flow separation, both the velocity and pressure contours provide consistent predictions. This suggests that within the laminar boundary layer, where the flow approaches equilibrium, the simple ALG can provide reasonably accurate predictions.

Figures 8 and 9 show the wake velocity profiles obtained from three different wall models at  $x/D = 1.06, 1.54,$  and  $2.02$  within the wake region, and they are also compared with the PIV experimental data by Parnaudeau.<sup>31</sup> From Figs. 8(a) and 9(a), when  $h = 2^{nd}$ , the streamwise velocity profiles from all three wall models exhibit a

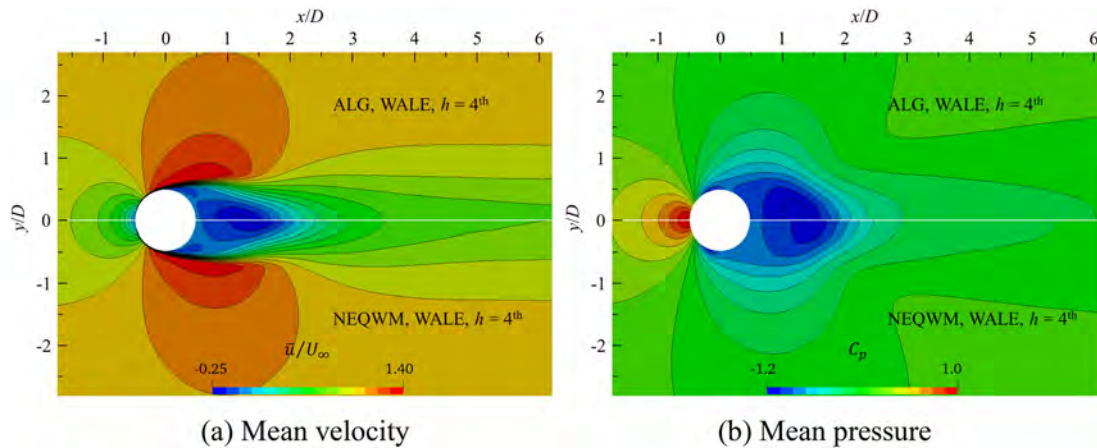


FIG. 7. Comparison of (a) mean velocity and (b) mean pressure contour normalized by  $U_{\infty}$  or  $U_{\infty}^2$ .



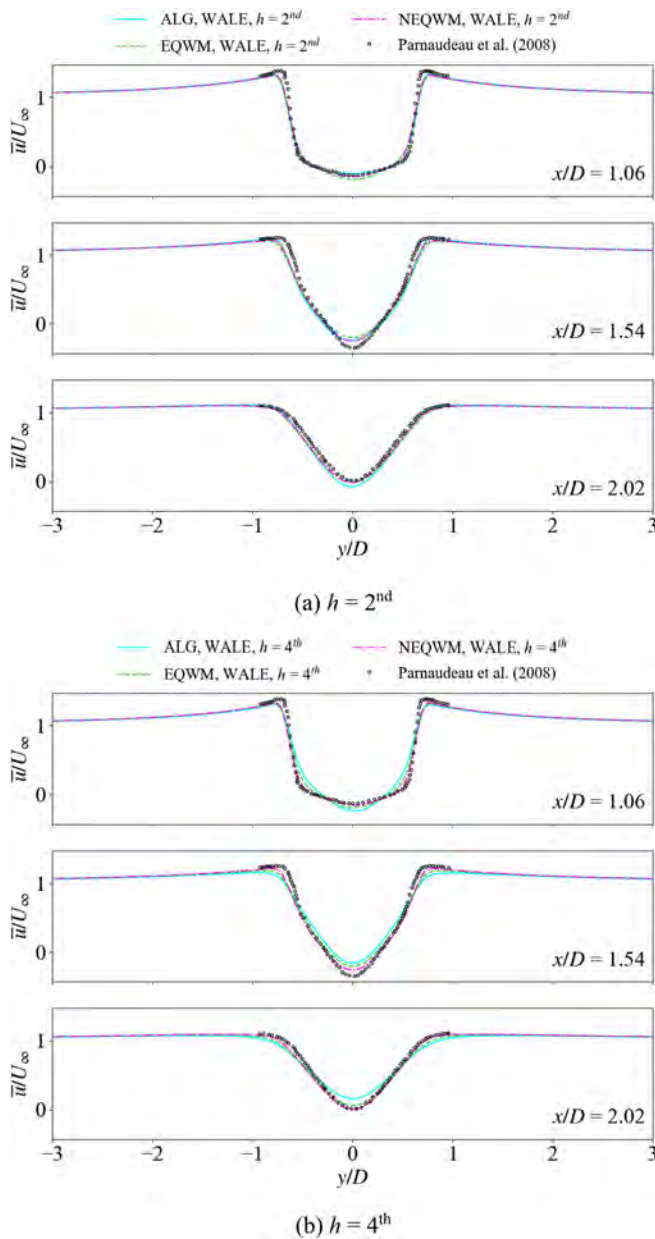


FIG. 8. Mean streamwise velocity profiles at  $x/D = 1.06, 1.54, \text{ and } 2.02$ .

U-shaped distribution, transitioning to a V-shaped distribution downstream. The transverse velocity profiles exhibit an anti-symmetric distribution. Among these, the results from the EQWM and NEQWM show a better agreement with the experimental data. The results from ALG show slight discrepancies but are satisfactory overall. Moving to Figs. 8(b) and 9(b), it can be observed when  $h = 4^{th}$ , the streamwise velocity profile obtained from the ALG presents a V-shaped distribution at  $x/D = 1.06$ . This is primarily due to errors in the prediction of the recirculation region length. In summary, at a larger sampling

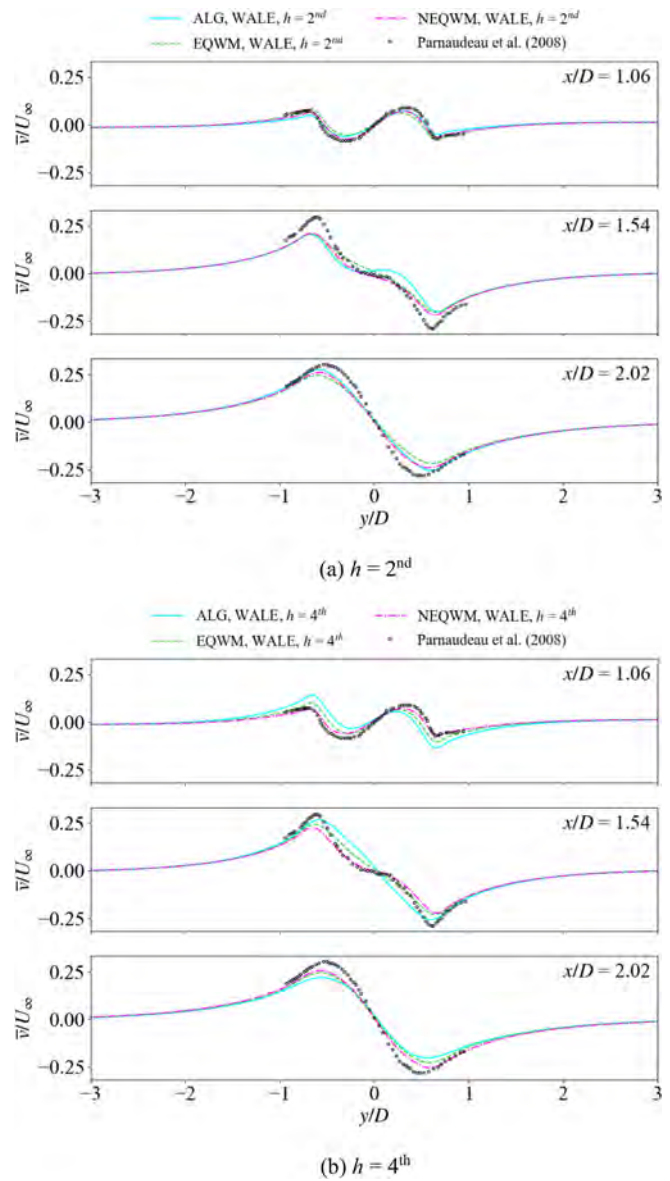
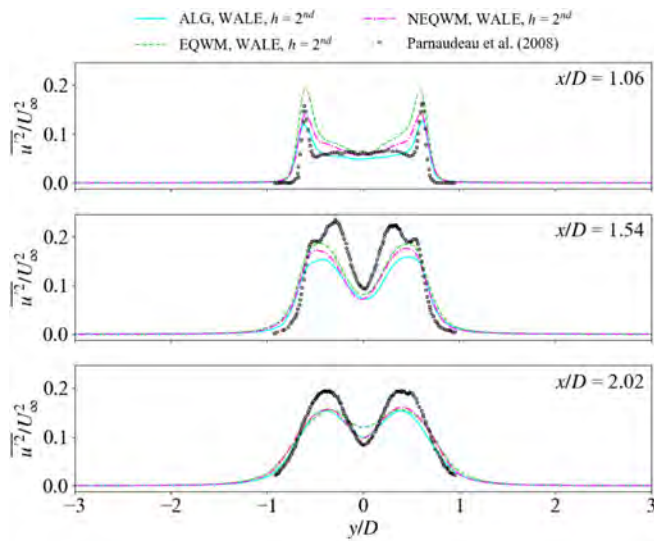


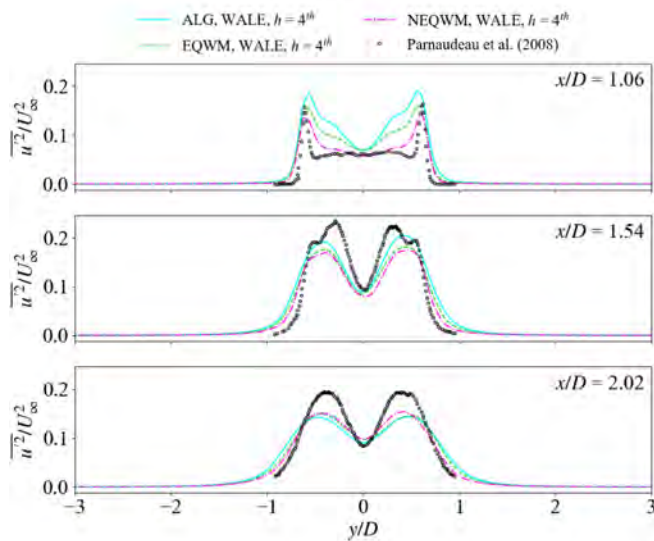
FIG. 9. Mean transverse velocity profiles at  $x/D = 1.06, 1.54, \text{ and } 2.02$ .

height, the NEQWM offers a more accurate prediction of the wake velocity profiles.

Figures 10–12 show the Reynolds stresses obtained from the three wall models within the wake at  $x/D = 1.06, 1.54, \text{ and } 2.02$ . The results are compared with PIV experimental data by Parnaudeau.<sup>31</sup> The Reynolds stress component  $\overline{u'u'}$  exhibits a bimodal distribution with the peaks corresponding to the positions of the shear layers. In the very near wake region, the predicted Reynolds stress is in reasonable agreement with the experimental data. However, at  $x/D = 1.54$  and  $2.02$ , the Reynolds stress overall underpredicted. This phenomenon has been observed in other numerical simulations.<sup>23,36,47</sup>

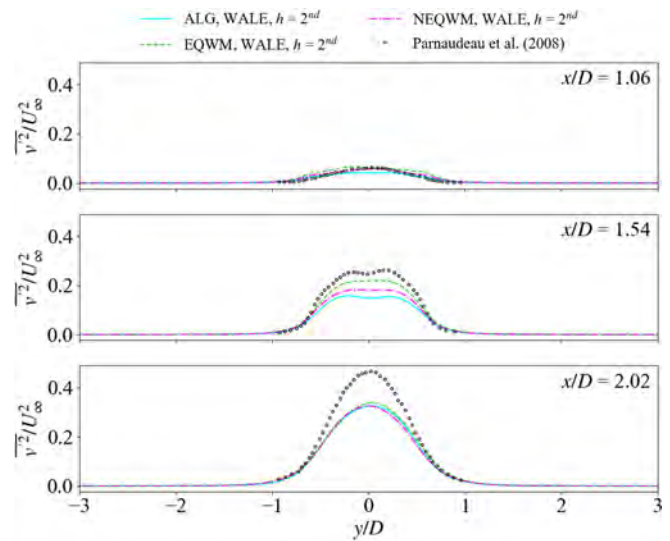


(a)  $h = 2^{nd}$

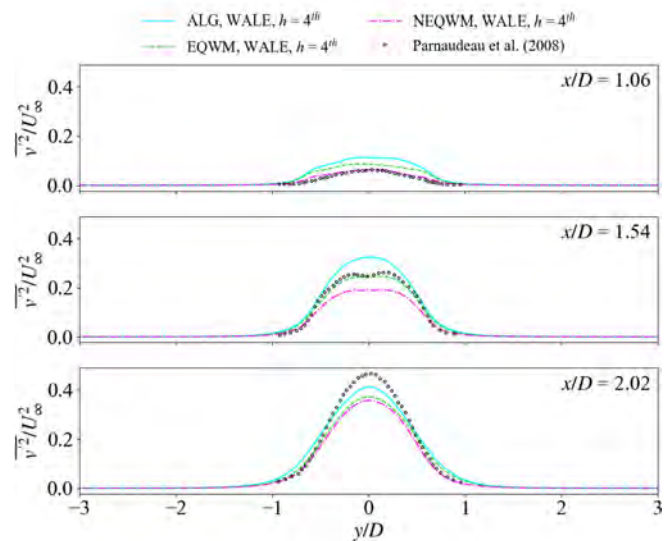


(b)  $h = 4^{th}$

FIG. 10. Mean resolved Reynolds stress  $\overline{u'u'}$  at  $x/D = 1.06, 1.54,$  and  $2.02$ .



(a)  $h = 2^{nd}$



(b)  $h = 4^{th}$

FIG. 11. Mean resolved Reynolds stress  $\overline{v'v'}$  at  $x/D = 1.06, 1.54,$  and  $2.02$ .

From Figs. 10(b), 11(b), and 12(b), it can be observed that at a larger sampling height, both the ALG and EQWM exhibit significant discrepancies. Particularly in Fig. 11(b), at  $x/D = 1.54$ , the EQWM appears to match the experimental Reynolds stress well. The underestimation of the recirculation length and the effect of numerical dissipation may compensate each other, causing an erroneous agreement with the experimental data.

Figure 13 shows the contours of the transverse velocity and Reynolds stress obtained from the NEQWM at  $h = 4^{th}$ . In these figures, the three white lines represent the wake cross sections at

$x/D = 1.06, 1.54,$  and  $2.02$ . The contour of the transverse velocity in Fig. 13(a) corresponds to the data shown in Fig. 9(b). Similarly, the three contours of Reynolds stress in Figs. 13(b)–13(d) correspond to the computational results presented in Figs. 10(b), 11(b), and 12(b), respectively. From the contours, we can observe that the transverse velocity and the resolved Reynolds stress  $\overline{u'v'}$  exhibit an anti-symmetric shape. The contour of the transverse velocity resembles the shape of a “butterfly.” In addition, the contours of  $\overline{u'u'}$  and  $\overline{v'v'}$  display symmetric distributions. For  $\overline{u'u'}$ , there are two maxima on either side of the wake centerline,

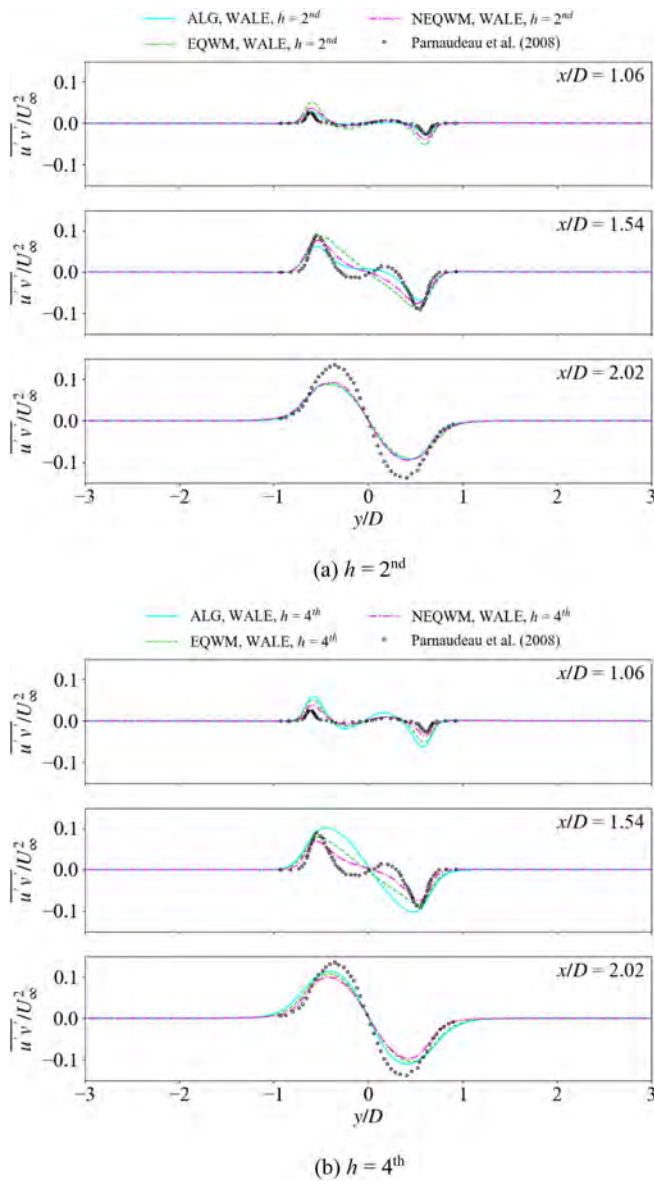


FIG. 12. Mean resolved Reynolds stress  $\overline{u'v'}$  at  $x/D = 1.06, 1.54,$  and  $2.02$ : (a)  $h = 2^{nd}$  and (b)  $h = 4^{th}$ .

corresponding to the free shear layer. The  $\overline{v'v'}$  has a single maximum, positioned along the wake centerline.

Figure 14 shows the instantaneous vortical structures of the flow past the cylinder obtained from NEQWM at  $h = 4^{th}$ , using the iso-surface of  $\Omega_R = 0.52$ <sup>48–50</sup> by the contour of Omega-Liutex. The visualization is colored by the dimensionless instantaneous streamwise velocity. Through the three-dimensional vortical structures, we can distinctly observe the laminar boundary layer of the cylinder flow, vortex shedding points, the free shear layer formed after flow separation, and the Karman vortex street within the wake.

In terms of turbulence fluctuations, Figs. 15 and 16 show the power spectra of velocity fluctuations at the location  $(x/D, y/D) = (3, 0)$  in the wake of a cylinder. The available sample count is 18 000, corresponding to a duration of  $T = 702D/U_\infty$ , which is approximately 175 shedding cycles. Figure 15 shows the streamwise velocity fluctuation power spectrum obtained from the three wall models, which exhibit a decay trend of  $-5/3$  (i.e., the inertial subrange). Figure 16 shows the transverse velocity fluctuation power spectrum. The abscissa at the peak of the power spectrum corresponds to the non-dimensional shedding frequency  $St$ . In Fig. 16(a), for  $h = 2^{nd}$ , the  $St$  of ALG, EQWM, and NEQWM are 0.204, 0.202, and 0.205, respectively. In Fig. 16(b), for  $h = 4^{th}$ , the  $St$  are 0.199, 0.198, and 0.207, respectively. When the sampling height is higher, the results from the NEQWM closely match the experimental data of Parnaudeau,<sup>31</sup> with  $St = 0.208 \pm 0.002$ , while the  $St$  predicted by the ALG and EQWM are smaller. Furthermore, in the power spectrum of the transverse velocity fluctuations, we observe the fundamental and second harmonic peaks at  $f_{vs}$  and  $3f_{vs}$ , respectively, which closely agree with the flow phenomena observed in experiments.<sup>30,31</sup> In the power spectrum of the streamwise velocity fluctuations, due to the symmetry conditions, only one prominent peak at  $2f_{vs}$  should exist at the centerline.<sup>41</sup> In the current study, the peak at  $2f_{vs}$  is indeed well captured.

### B. Effect of SGS models

In this part, we study the effect of different SGS models, namely, the SMAG model, the KSGS model, the WALE model, the DSMAG model, and the DKSGS model. Since the results of different wall models have demonstrated that the NEQWM provides the most ideal numerical simulation results, tests of different SGS models are conducted using the NEQWM and the sampling height is  $h = 4^{th}$  in this part.

Table V provides a comparison of the computational cost and efficiency of different SGS models. Each case was simulated for 780 dimensionless time units, with same partitioning strategy. The ranking of computational cost from lowest to highest is as follows: SMAG, KSGS, WALE, DSMAG, and DKSGS. Using the computational efficiency of the SMAG model as the baseline, the computational cost of dynamic SGS models is notably higher than that of static SGS models. The WALE model falls between the two in terms of computational cost.

Table VI provides the statistical flow quantities for cylinder flow obtained from five different SGS models. In terms of the forces acting on the cylinder, Fig. 17 shows the time history curves of lift and drag coefficients computed by five SGS models. Among these curves, those oscillating around 1 represent the drag coefficient time history, while those oscillating around 0 represent the lift coefficient time history. From the time history curves, it can be observed that moments with higher drag coefficients generally correspond to larger lift coefficient magnitudes, aligning well with experimental and DNS predictions. Considering the values in Table VI for  $\overline{C_d}$  and  $(C_l)_{rms}$ , it is evident that different SGS models provide reasonably accurate predictions for lift and drag forces.

Figure 18 shows the surface pressure distribution around the cylinder, and we compare it with the experimental data from Lourenco<sup>28</sup> and Norberg.<sup>29</sup> By comparing the results, we can observe that the curve of the KSGS model is lower than the experimental data in the range of  $50^\circ - 100^\circ$ , while the rest of the SGS models show good overall

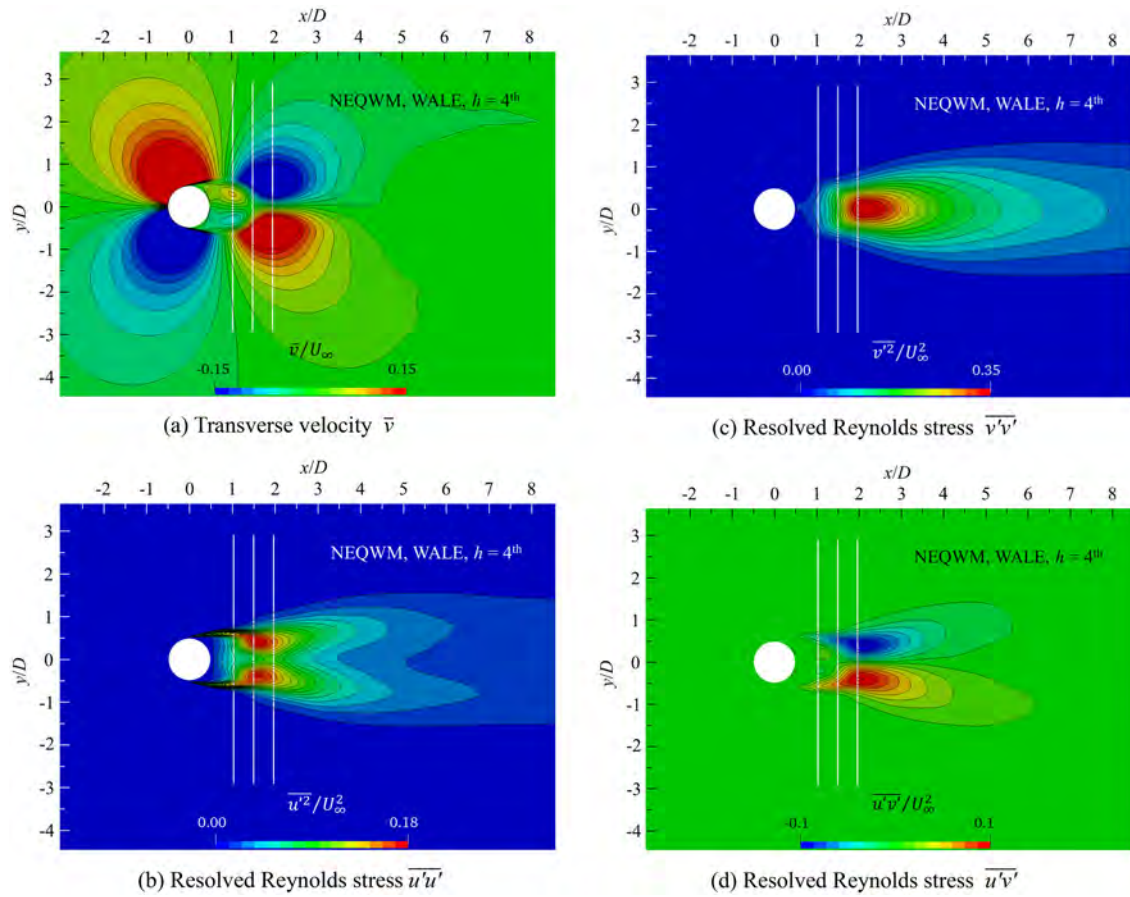


FIG. 13. (a) Mean transverse velocity  $\bar{v}$  and resolved Reynolds stress (b)  $\overline{u'u'}$ , (c)  $\overline{v'v'}$ , and (d)  $\overline{u'v'}$  contours normalized by  $U_\infty$  or  $U_\infty^2$ .

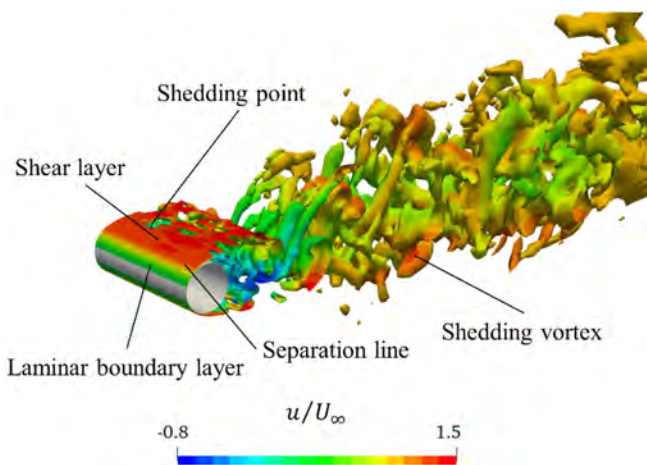


FIG. 14. Instantaneous three-dimension vortical structures of the flow past the cylinder:  $\Omega_R = 0.52$ .

agreement. From Table VI, it is evident that the pressure coefficients  $C_{pb}$  at the cylinder's rear end computed by the KSGS and SMAG models are slightly lower than the experimental data, which contributes to the slightly lower time-averaged drag coefficient.

In terms of flow separation prediction, Fig. 19 shows the time-averaged wall-normal velocity gradients on the cylinder surface predicted by different SGS models. Considering the flow separation angles provided in Table VI, it can be observed that on the front half of cylinder, the SMAG and KSGS models yield relatively large surface velocity gradients and consequently predict larger flow separation angles, indicating a significant delay in flow separation. Due to the fact that the coefficients of the SMAG and KSGS models are constants, their accuracy near the wall is noticeably lower. The SGS eddy viscosity near the wall is overestimated, resulting in higher dissipation, which falsely suppresses the occurrence of flow separation. Compared with the static SGS models, the two dynamic SGS models provide more accurate flow separation angles. In addition, since the WALE model inherently accounts for wall effects in turbulence, it also offers accurate predictive outcomes.

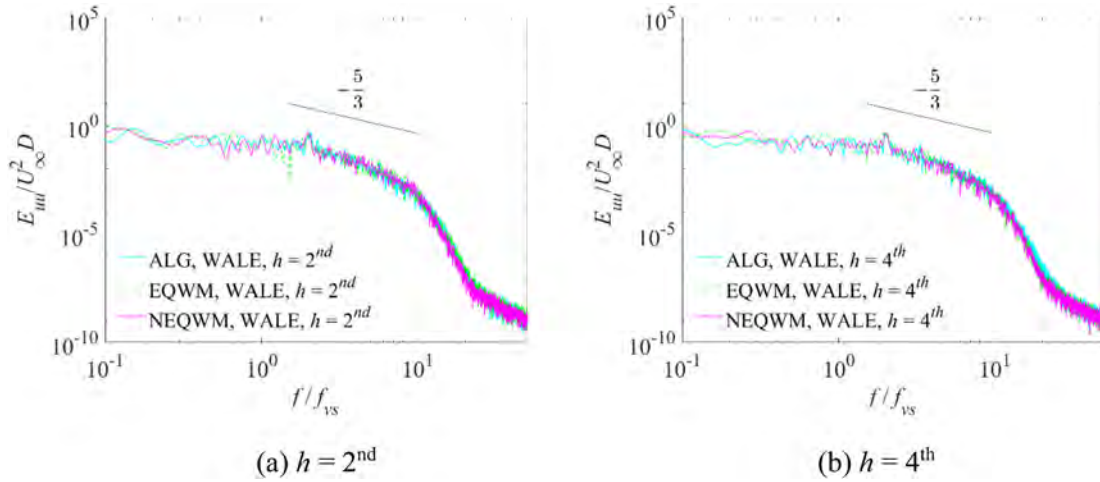


FIG. 15. Power spectra of the streamwise velocity fluctuations at  $(x/D, y/D) = (3, 0)$  in the wake.

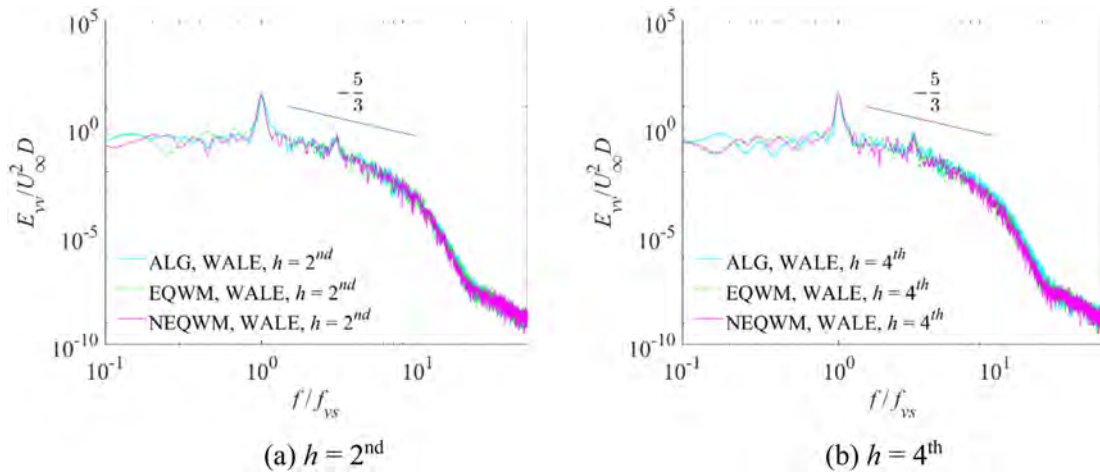


FIG. 16. Power spectra of the transverse velocity fluctuations at  $(x/D, y/D) = (3, 0)$  in the wake.

TABLE V. Computational cost and efficiency of different SGS models.

Case	Computational cost (s)	Computation efficiency (%)
NEQWM, SMAG, $h = 4^{\text{th}}$	64 374	100
NEQWM, KSGS, $h = 4^{\text{th}}$	66 867	103.8
NEQWM, WALE, $h = 4^{\text{th}}$	67 031	104.1
NEQWM, DSMAG, $h = 4^{\text{th}}$	68 988	107.2
NEQWM, DKSGS, $h = 4^{\text{th}}$	72 229	112.2

In terms of the prediction of recirculation length, Fig. 20(a) shows the streamwise velocity profiles along the wake centerline. Combining the profile with the values  $L_{rec}/D$  in Table VI, it can be observed that the DSMAG model predicts a larger recirculation length, while the

KSGS model yields a relatively smaller wake length. The other three SGS models produce more accurate results. In Fig. 20(b), the Reynolds stress profiles along the wake centerline are presented. The results obtained by the SMAG and KSGS models are lower than the experimental data, indicating higher dissipation in these two SGS models. Additionally, considering the peak position of Reynolds stress, we can also observe that the DSMAG model overestimates the wake length of the cylinder.

Figure 21 shows the wake velocity profiles predicted by the different SGS models at  $x/D = 1.06, 1.54,$  and  $2.02$ , together with PIV experimental data from Parnaudeau.<sup>31</sup> The streamwise velocity profiles from five SGS models exhibit a U-shaped distribution initially and transition to a V-shaped distribution downstream. The transverse velocity profiles show anti-symmetric distributions. The overall computational results show good agreement with the experimental data, indicating that both dynamic and static SGS models yield satisfactory results in regions away from the wall.

TABLE VI. Statistical flow quantities for flow past a cylinder.

Data from	$\bar{C}_d$	$(C_l)_{rms}$	$-\bar{C}_{pb}$	$L_{rec}/D$	$\theta_{sep}$ (deg)	$St$
Lourenco <sup>28</sup> (Exp)	0.99	...	...	1.19	86	0.22
Norberg <sup>29</sup> (Exp)	0.98	0.04	0.90	...	...	...
		-0.15				
Parnaudeau <i>et al.</i> <sup>31</sup> (Exp)	...	...	...	1.51	88	0.208
Ma <i>et al.</i> <sup>41</sup> (DNS)	...	...	0.84	1.59	88	0.219
Tian and Xiao <sup>42</sup> (LES)	0.98	...	0.85	1.64	88	...
Ren <i>et al.</i> <sup>23</sup> (WMLLES)	1.000	0.104	0.824	1.662	88.81	0.209
NEQWM, SMAG, $h = 4^{th}$	0.980	0.103	0.859	1.540	95.209	0.214
NEQWM, KSGS, $h = 4^{th}$	0.977	0.119	0.873	1.437	97.140	0.218
NEQWM, WALE, $h = 4^{th}$	1.020	0.149	0.908	1.519	85.914	0.207
NEQWM, DSMAG, $h = 4^{th}$	1.003	0.119	0.888	1.638	85.713	0.205
NEQWM, DKSGS, $h = 4^{th}$	1.019	0.137	0.912	1.535	85.894	0.204

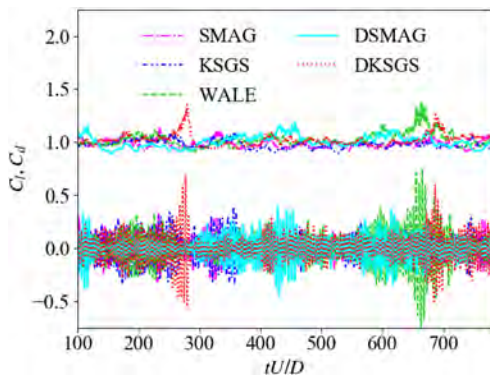


FIG. 17. Time history of lift and drag force for the cylinder.

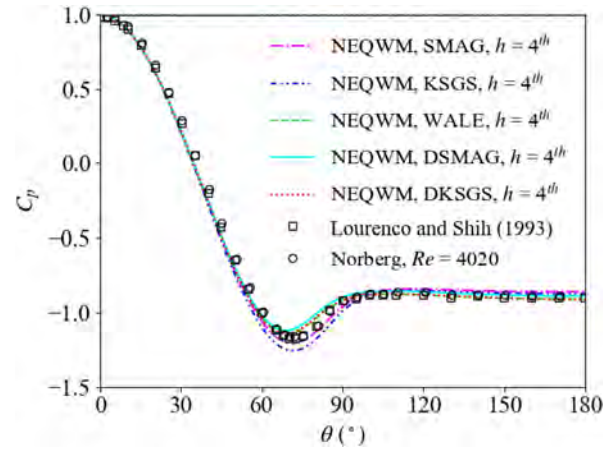


FIG. 18. Mean pressure distribution on the cylinder surface by different SGS models.

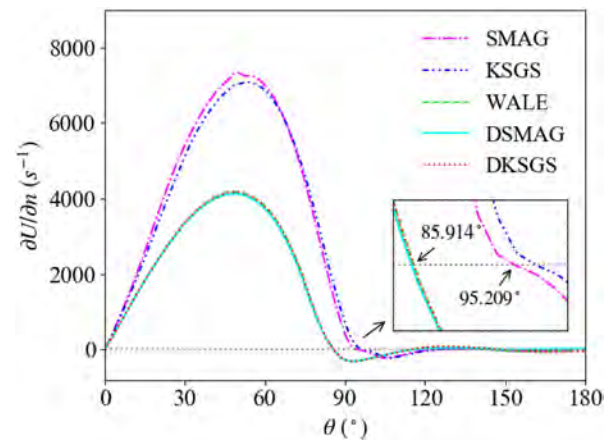


FIG. 19. Wall-normal velocity gradients calculated by different SGS models.

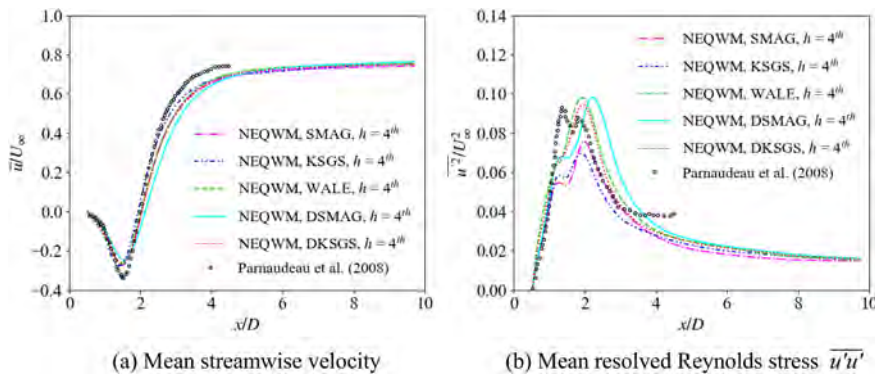


FIG. 20. (a) Mean streamwise velocity and (b) mean Reynolds stress along wake centerline by different SGS models.

08 February 2024 14:35:45

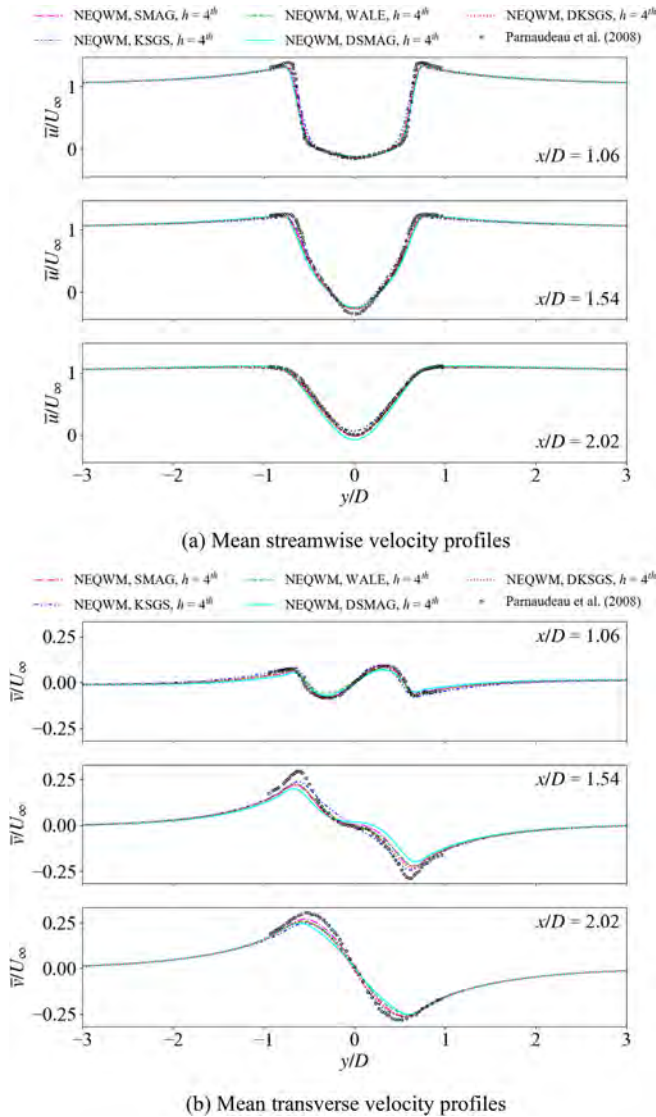


FIG. 21. (a) Mean streamwise velocity and (b) mean transverse velocity profiles at  $x/D = 1.06, 1.54,$  and  $2.02$ .

Figure 22 shows the dimensionless resolved Reynolds stress at  $x/D = 1.06, 1.54,$  and  $2.02$  in the wake predicted by the five SGS models together with PIV experimental data from Parnaudeau.<sup>31</sup> The Reynolds stress  $\overline{u'u'}$  exhibits a double-hump shape, with the positions of the humps corresponding to the shear layer locations. By comparing the Reynolds stress  $\overline{u'u'}$  at  $x/D = 1.06$ , it is evident that the results from the SMAG and KSGS models are lower than the experimental data at the shear layers, and the peak Reynolds stresses calculated by the SMAG and KSGS models are underestimated by 47.8% and 40.5%, respectively, compared to the experimental data. The main reason is that the LES model coefficient is problem-dependent. For local complex flows like free shear flow, constant model coefficients inevitably lead to computational errors, resulting in computed Reynolds stress

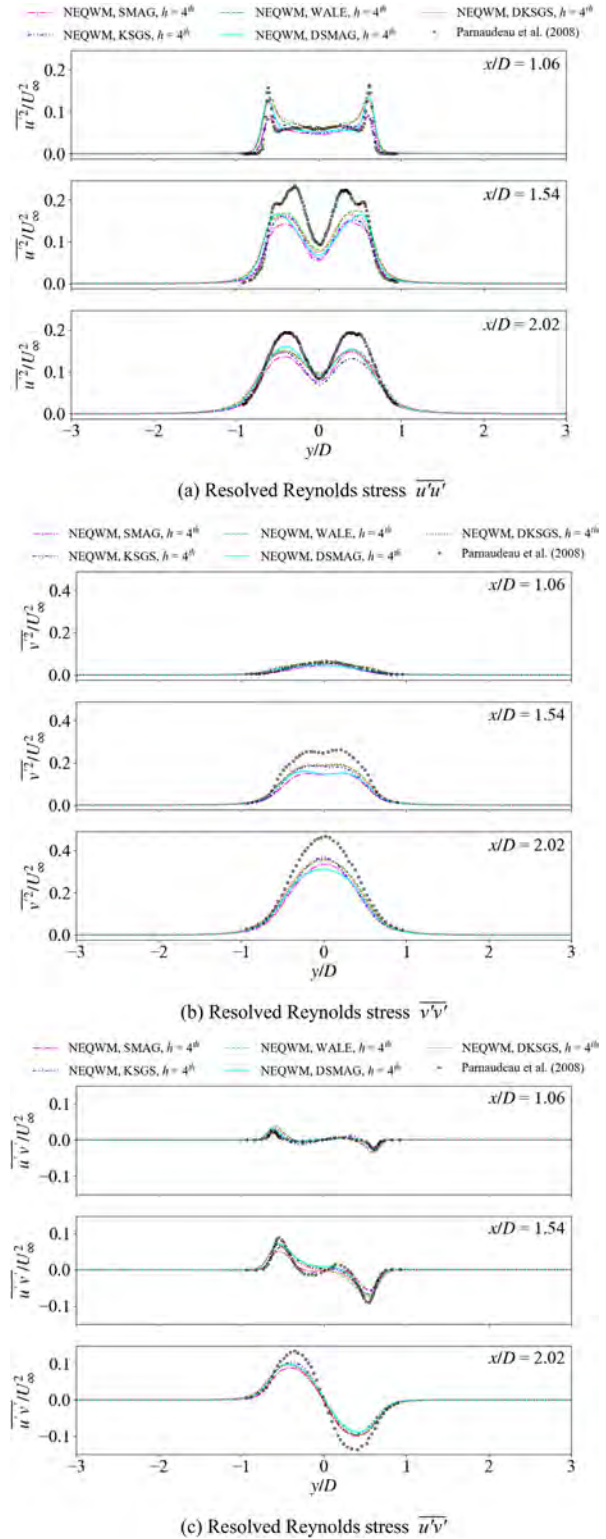


FIG. 22. Mean resolved Reynolds stress: (a)  $\overline{u'u'}$ , (b)  $\overline{v'v'}$ , and (c)  $\overline{u'v'}$  at  $x/D = 1.06, 1.54,$  and  $2.02$ .

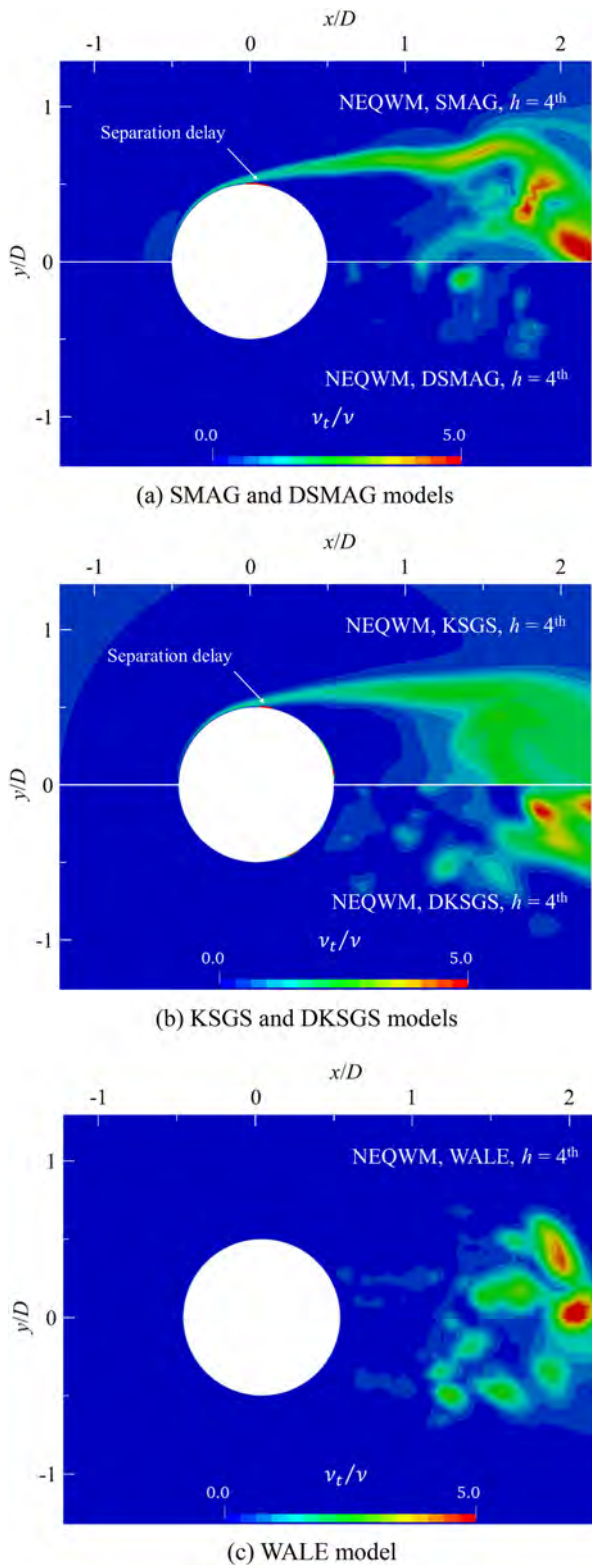


FIG. 23. Comparison of turbulent eddy viscosity of different SGS models.

values lower than the experimental data. The other three SGS models show better agreement with the experimental data at  $x/D = 1.06$ . Additionally, in the downstream part of the wake, the lower resolution in the  $x$ - $y$  plane and relatively higher dissipation lead to the overall computed Reynolds stress profiles being lower than the experimental data.

Figures 23(a) and 23(b), respectively, show the comparison of turbulent eddy viscosity between SMAG and DSMAG models and KSGS and DKSGS models. Figure 23(c) shows the result of WALE model. These values have been non-dimensionalized and are represented by 16 contours of  $\nu_t/\nu$  ranging from 0 to 5. It is evident that the SMAG and KSGS models, compared to the dynamic SGS models, exhibit significantly higher turbulent eddy viscosity near the wall and within the free shear layers. This inevitably leads to higher turbulence dissipation, which is a primary reason for the substantial deviation in the resolved Reynolds stress  $\overline{u'u'}$ , as shown in Fig. 22(a). In addition, it is worth noting that the WALE model does not encounter the issues observed in the near-wall and free shear layers as seen in the SMAG and KSGS models. The modification to the rate-of-strain tensor has been proven successful. Furthermore, for SMAG and KSGS models, we observed significantly elevated turbulence eddy viscosity near the point of flow separation, resulting in delayed flow separation due to increased turbulence dissipation. This further explains why both the static SGS models predict a larger flow separation angle. In summary, the static SGS models with constant model coefficients exhibit lower predictive accuracy near the wall and within the free shear layer.

Figure 24 provides the contours of instantaneous vorticity within the  $z = 0$  plane of the flow field. The plots display 16 contours of  $|\omega|D/U_\infty$  ranging from 0.5 to 10.0. The contours clearly depict the free shear layers on both sides of the cylinder as well as the Karman vortex street in the wake. The DKSGS model is able to resolve finer flow structures due to less dissipation. However, the capturing capability of small-scale turbulent structures is relatively weaker for the SMAG and DSMAG models. The overall computational results of the WALE and KSGS models lie between those of the DKSGS and SMAG models. This suggests that the DKSGS model, due to its incorporation of SGS turbulence energy transfer effects and dynamic coefficient selection, is a good choice for wall stress model.

Figure 25 shows the power spectra of velocity fluctuations at the downstream location  $(x/D, y/D) = (3, 0)$  for the five SGS models. A total of 18000 samples are used, corresponding to a duration of  $T = 702D/U_\infty$ , which is approximately 175 shedding cycles. Combining these data with the  $St$  values in Table VI, the  $St$  obtained from the SMAG, KSGS, WALE, DSMAG, and DKSGS models are 0.214, 0.218, 0.207, 0.205, and 0.204, respectively. Among these, the  $St$  predicted by the SMAG and KSGS models are higher than the experimental data, while the other three models show better agreement with the experimental data. Furthermore, in the predicted results of different SGS models, we observed both the fundamental and second harmonic in the  $v$ -spectra, located at  $f_{vs}$  and  $3f_{vs}$ , respectively. In the  $u$ -spectra, we also observed a peak at  $2f_{vs}$ .

IV. CONCLUSION

In this paper, based on the open-source computational fluid dynamics platform OpenFOAM, we conducted numerical investigations of the flow past a cylinder at subcritical Reynolds numbers  $Re_D = 3900$ . To comprehensively evaluate the performance of the ALG, EQWM, and NEQWM in flow separation, a systematic



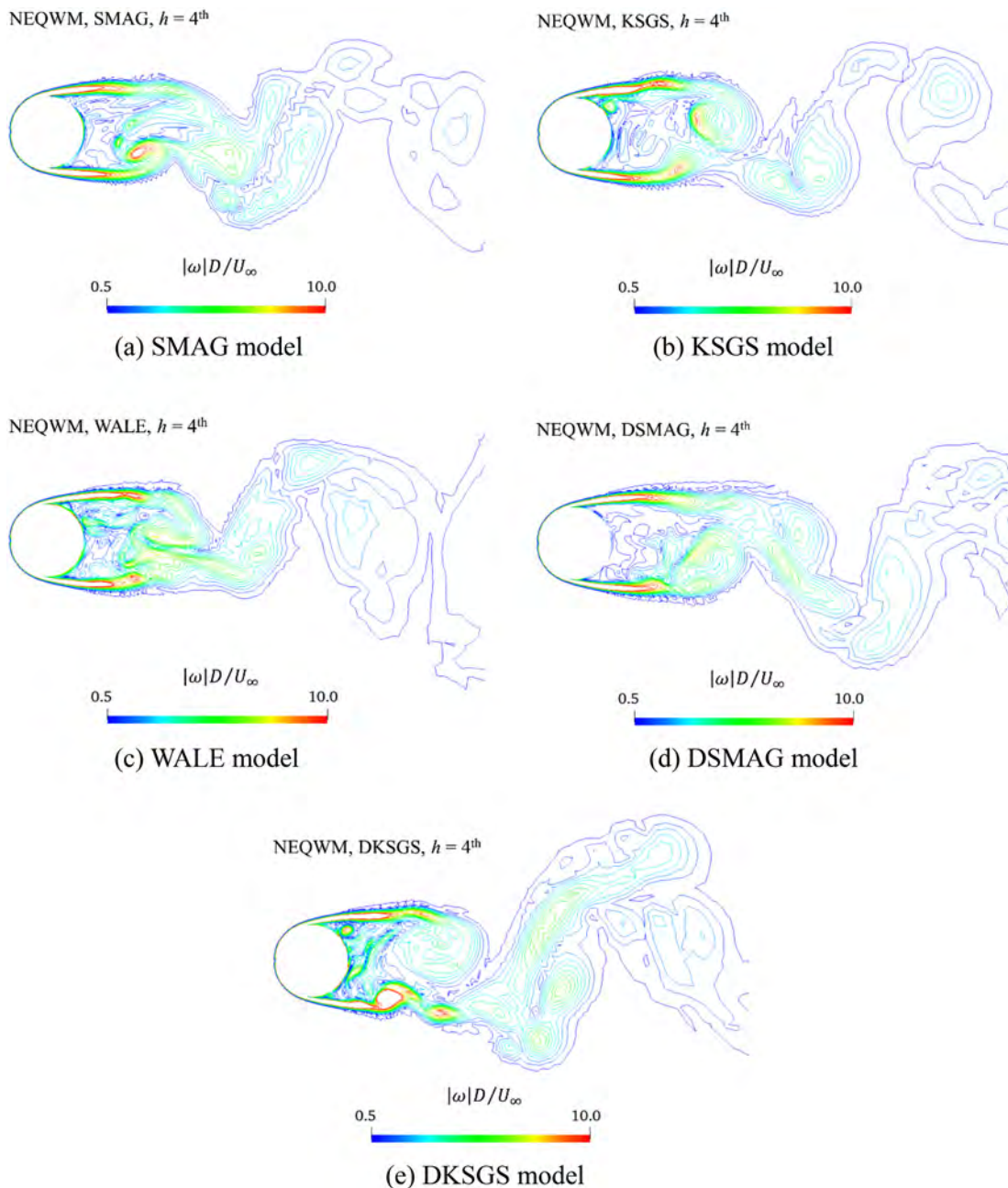


FIG. 24. Instantaneous vorticity magnitude ( $|\omega|D/U_\infty$ ), shown by 16 contours from 0.5 to 10.0, obtained by different SGS models.

comparison of three wall models was carried out at two different sampling heights ( $h = 2^{\text{nd}}$  and  $h = 4^{\text{th}}$ ). Meanwhile, we also compared the effect of five SGS models used in the wall stress model and their performance in flow separation, namely, the SMAG model, the KSGS model, the WALE model, the DSMAG model, and the DKSGS model. We analyzed the forces acting on the cylinder, flow separation, velocity profiles of the wake, and Reynolds stresses and compared the results

with the experimental data. We also focused on the vortex system structure, the turbulent eddy viscosity around the cylinder, and the velocity fluctuations in the wake. The main conclusions drawn from this study are as follows.

In terms of predictive accuracy among different wall models, all three types of wall models yield relatively accurate predictions when the sampling height is set to  $h = 2^{\text{nd}}$ . Among them, the ALG slightly

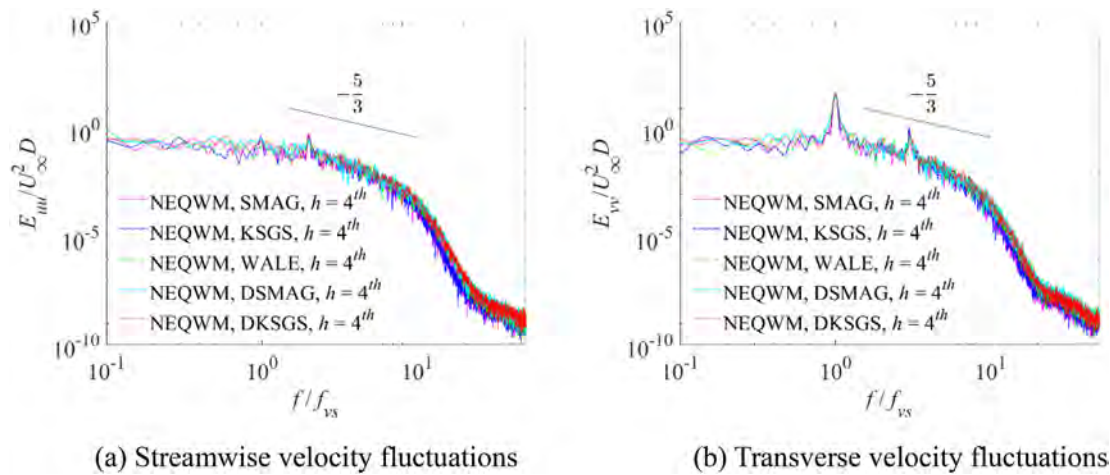


FIG. 25. Power spectra of the (a) streamwise velocity and (b) transverse velocity fluctuations at  $(x/D, y/D) = (3, 0)$  in the wake.

overestimates the length of the recirculation region by 8.5%, but the overall computational precision is acceptable. When  $h = 4^{\text{th}}$ , the non-equilibrium phenomena in the flow at those sampling heights appear to be more pronounced. In this scenario, the NEQWM still provides fairly accurate predictions of the recirculation region length, with only a 0.6% difference compared to the experimental data. However, the ALG and the EQWM exhibit a noticeable decrease in the overall computational accuracy. Both the two models underestimate the length of the recirculation region, with underestimations of 14.8% and 5%, respectively, leading to discrepancies in the velocity profile of the wake and the Reynolds stress distribution. The negative pressures at the rear of the cylinder obtained from the ALG and the EQWM are overestimated by 12.8% and 6.8%, respectively, leading to a significant increase in cylinder lift and drag forces. In terms of velocity fluctuations, all the power spectra effectively capture a narrow inertial subrange and exhibit characteristic peaks associated with the vortex shedding frequency. When  $h = 4^{\text{th}}$ , the  $St$  obtained from the ALG and the EQWM are underestimated by 4.3% and 4.8%, respectively. However, the result of NEQWM agrees with the experimental data well.

The turbulent temporal and spatial scales are directly proportional to the distance from the wall. As one gets closer to the wall, the turbulent scales become smaller. Moreover, due to the no-slip velocity boundary condition on the wall, the convection term becomes negligible. The pressure gradient term gradually diminishes to zero closer to the wall on account of the zero-gradient pressure boundary condition on the wall. In the vicinity of the wall, it is reasonable to assume that the effects of the convection term and the pressure gradient term compensate each other, resulting in a nearly equilibrium flow state. Consequently, at smaller sampling heights, the ALG and the EQWM provide more accurate simulation results. However, as the sampling height increases, the sampled points move away from the wall. In such situations, the equilibrium state of the flow could potentially be disrupted. This disruption is particularly evident in cases of strong separated flows, such as the flow around a cylinder, where the impact of the pressure gradient term becomes more significant. Here, the NEQWM, compared to the other two wall models, offers more precise numerical simulation results. Importantly, the NEQWM is less sensitive to the

choice of sampling height, at least for the physical quantities compared in this paper, showcasing a high level of robustness.

In terms of the effects of different SGS models, we observe that the drag and lift forces on the cylinder, as well as the surface pressure distribution, are not particularly sensitive to the choice of SGS models. However, in predicting flow separation, the SMAG model and KSGS model, due to their constant model coefficients, exhibit a noticeable decrease in the computational accuracy near the wall. The flow separation angles obtained from SMAG model and KSGS model are overestimated by 8.2% and 10.4%, respectively, showing a significant delay of flow separation. In the wake region far away from the wall, all the different SGS models provide reasonably accurate velocity profiles. However, in validating the wake Reynolds stress, we find that the Reynolds stresses predicted by different SGS models are consistently lower than the experiment data. The peaks of Reynolds stress at the shear layer predicted by SMAG model and KSGS model are underestimated by 47.8% and 40.5%, respectively. The results of WALE model, DSMAG model, and DKSGS model are underestimated by 13.3%, 17.9%, and 18.7%, respectively. One possible reason for this discrepancy could be insufficient grid resolution. On the other hand, it also indicates the inherent limitations of static SGS models. Compared with the DSMAG and DKSGS models, the two static models exhibit higher SGS eddy viscosity in free shear flows, leading to increased numerical dissipation. Meanwhile, the WALE model's SGS eddy viscosity automatically approaches zero in pure shear flow regions, and its results agree well with experimental data too. Overall, when considering different SGS models in conjunction with wall stress models, the dynamic SGS models and the WALE model are preferred over the static SGS models, such as the SMAG model and KSGS model. However, the computational cost of the WALE model is lower in actual computations compared to dynamic SGS models, and in high Reynolds number flows, the improvement in the computational efficiency might be more pronounced.

## ACKNOWLEDGMENTS

This authors acknowledge the financial support from the National Key Research and Development Program of China (No.

2022YFC2806705) and the National Natural Science Foundation of China (Grant Nos. 51909160 and 52131102). We express our gratitude for the provided funding.

**AUTHOR DECLARATIONS**

**Conflict of Interest**

The authors have no conflicts to disclose.

**Author Contributions**

**Guoqing Fan:** Conceptualization (equal); Formal analysis (equal); Investigation (equal); Methodology (equal); Validation (equal); Visualization (equal); Writing – original draft (equal). **Yuan Liu:** Investigation (equal); Validation (equal); Visualization (equal); Writing – review & editing (equal). **Weiwen Zhao:** Conceptualization (lead); Data curation (equal); Funding acquisition (equal); Investigation (equal); Methodology (equal); Project administration (equal); Supervision (equal); Validation (equal); Writing – review & editing (equal). **Decheng Wan:** Funding acquisition (lead); Resources (lead); Supervision (lead); Writing – review & editing (equal).

**DATA AVAILABILITY**

The data that support the findings of this study are available from the corresponding author upon reasonable request.

**APPENDIX A: SGS MODELS**

**1. Smagorinsky model**

For the SMAG model,<sup>1</sup> we use SGS kinetic energy for calculations and the formula for SGS eddy viscosity is given by

$$\nu_{sgs} = C_k \Delta \sqrt{k_{sgs}}, \tag{A1}$$

where  $\Delta$  is the cube root of local cell volume. The SGS kinetic energy  $k_{sgs}$  is obtained by the local equilibrium assumption (the production rate equals the dissipation rate),

$$k_{sgs} = \frac{C_k \Delta^2 |\tilde{S}_{ij}|^2}{C_e}, \tag{A2}$$

where  $C_k = 0.094$  and  $C_e = 1.048$  are the model constants and  $|\tilde{S}_{ij}| = \sqrt{2\tilde{S}_{ij}\tilde{S}_{ij}}$  is the magnitude of the resolved strain rate tensor.

**2. k-equation model**

As the one-equation SGS models, the KSGS model<sup>6</sup> considers the transport process of SGS kinetic energy. The development of this type of SGS model is mainly aimed at overcoming the deficiencies of the local equilibrium assumption between energy production and dissipation in algebraic eddy viscosity models, particularly for high Reynolds number flows and insufficient grid resolution. The transport equation for  $k_{sgs}$  can be obtained by solving the following equation:

$$\frac{\partial k_{sgs}}{\partial t} + \frac{\partial \tilde{u}_j k_{sgs}}{\partial x_j} - \frac{\partial}{\partial x_j} \left( \nu + \nu_{sgs} \frac{\partial k_{sgs}}{\partial x_j} \right) = -\tau_{ij} : \tilde{S}_{ij} - C_e \frac{k_{sgs}^{3/2}}{\Delta}, \tag{A3}$$

where  $C_k = 0.094$  and  $C_e = 1.048$  are model constants. The SGS eddy viscosity in this model is also provided by Eq. (A1).

**3. Wall-adapting local eddy-viscosity model**

The WALE model<sup>5</sup> modifies the strain rate tensor term and take the rotation rate into account. The formula for calculating the SGS eddy viscosity is as follows:

$$\nu_{sgs} = (C_w \Delta)^2 \frac{(S_{ij}^d S_{ij}^d)^{3/2}}{(\tilde{S}_{ij} \tilde{S}_{ij})^{5/2} + (S_{ij}^d S_{ij}^d)^{5/4}}, \tag{A4}$$

$$S_{ij}^d = \frac{1}{2} \left( \frac{\partial \tilde{u}_i}{\partial x_k} \frac{\partial \tilde{u}_k}{\partial x_j} + \frac{\partial \tilde{u}_j}{\partial x_k} \frac{\partial \tilde{u}_k}{\partial x_i} \right) - \frac{1}{3} \delta_{ij} \frac{\partial \tilde{u}_k}{\partial x_l} \frac{\partial \tilde{u}_l}{\partial x_k}, \tag{A5}$$

where  $C_w = 0.325$  is the WALE coefficient and  $S_{ij}^d$  is the traceless symmetric part of the square of the velocity gradient tensor. The WALE model is automatically setting the  $\nu_{sgs}$  to zero in pure shear flow regions, and damping is not necessary for  $\nu_{sgs}$  in the near-wall region.

**4. Dynamic Smagorinsky model**

The DSMAG model,<sup>3,4</sup> as a dynamic SGS model, dynamically selects the model coefficient by employing a secondary filtering of the flow field, also known as the test filter. The SGS eddy viscosity is given by

$$\nu_{sgs} = (C_s \Delta)^2 |\tilde{S}_{ij}|, \tag{A6}$$

where the model coefficient  $C_s$  is dynamically selected by

$$C_s^2 = \frac{1}{2} \frac{L_{ij} M_{ij}}{M_{kl} M_{kl}}. \tag{A7}$$

Here,  $L_{ij}$  is the resolved stress tensor, which can be calculated by the Germano identity,

$$L_{ij} = \widehat{\tilde{u}_i \tilde{u}_j} - \tilde{u}_i \tilde{u}_j. \tag{A8}$$

$M_{ij}$  is calculated by

$$M_{ij} = 2\Delta^2 |\widehat{\tilde{S}_{ij}}| \widehat{\tilde{S}_{ij}} - 2\widehat{\Delta}^2 |\widehat{\tilde{S}_{ij}}| \widehat{\tilde{S}_{ij}}, \tag{A9}$$

where  $\widehat{\Delta}$  represents the width of the test filter, which is twice the width of the grid filter.

**5. Dynamic k-equation model**

For the DKSGS model,<sup>7</sup> the SGS eddy viscosity is also provided by Eq. (A1). However, the model coefficients  $C_k$  and  $C_e$  are dynamically evaluated, which are similar to those in the DSMAG model,

$$C_k = \frac{1}{2} \frac{L_{ij} M_{ij}}{M_{kl} M_{kl}}, \tag{A10}$$

$$C_e = \frac{(\nu + \nu_{sgs}) (\widehat{\tilde{S}_{ij}} \widehat{\tilde{S}_{ij}} - \widehat{\tilde{S}_{ij}} \widehat{\tilde{S}_{ij}}) \widehat{\Delta}}{k_{test}^{3/2}}. \tag{A11}$$

Here,  $M_{ij}$  and  $k_{test}$  are given by

$$M_{ij} = -\sqrt{k_{test}} \widehat{\tilde{S}_{ij}} \widehat{\Delta}, \tag{A12}$$

$$k_{rest} = \frac{1}{2}(\widehat{u}_k \widehat{u}_k - \widehat{u}_k \widehat{u}_k). \quad (A13)$$

APPENDIX B: WALL MODELS

1. Algebraic model

The ALG is mainly based on the law of the wall, where the dimensionless velocity  $u^+ = u/u_\tau$  and the dimensionless wall-normal distance  $x_2^+ = x_2 u_\tau / \nu$  satisfy a linear relationship in the viscous sublayer and a logarithmic relationship in the logarithmic layer. The ALG employed in this study adopts Spalding’s law<sup>13</sup> for the law of the wall,

$$x_2^+ = \langle u \rangle^+ + e^{-\kappa B} \left[ e^{\kappa \langle u \rangle^+} - 1 - \kappa \langle u \rangle^+ - \frac{1}{2} (\kappa \langle u \rangle^+)^2 - \frac{1}{6} (\kappa \langle u \rangle^+)^3 \right], \quad (B1)$$

where Karman constant  $\kappa = 0.4$  and the constant  $B = 5.5$ . The brackets  $\langle \cdot \rangle$  denote averaging in time or ensemble. In ALG, the values of velocity are sampled from the cell center within the LES domain. The wall-normal distance from the sampling point to the wall is the sampling height,  $h$ . By solving the non-linear algebraic equation iteratively, the friction velocity  $u_\tau$  can be determined. Then, with the wall shear stress formula  $\tau_w = \rho u_\tau^2$ , the correct boundary conditions for wall shear stress can be obtained.

2. Equilibrium and non-equilibrium ODE-based wall models

For ODE-based wall models,<sup>14</sup> the starting point is the simplified TBLE. In the inner layer of the boundary layer, the pressure gradient in the wall-normal direction is assumed to be zero. As a result, the N-S equations within the boundary layer can be simplified as<sup>25</sup>

$$\frac{\partial}{\partial x_2} \left[ (\nu + \nu_t) \frac{\partial u_i}{\partial x_2} \right] = F_i, \quad i = 1, 3, \quad (B2)$$

where  $F_i$  is the source term,

$$F_i = \frac{1}{\rho} \frac{\partial p}{\partial x_i} + \frac{\partial u_i}{\partial t} + \frac{\partial}{\partial x_j} u_i u_j. \quad (B3)$$

The turbulent eddy viscosity is obtained from the mixing length theory<sup>2</sup> with a near-wall damping function,

$$\nu_t = \kappa \nu x_2^+ (1 - e^{-x_2^+/A})^2, \quad (B4)$$

where  $A = 17.8$ . The ODE-based wall models sample  $F_i$  from the LES domain, resulting in a constant source term. Equation (B2), then, degenerates into an ordinary differential equation. By integrating Eq. (B2) from the wall to the sampling point, the boundary condition for wall shear stress can be obtained as

$$\tau_{wi} = \mu \frac{\partial u_i}{\partial x_2} \Big|_{x_2=0} = \frac{\rho}{\int_0^h \frac{dx_2}{\nu + \nu_t}} \left\{ u_{hi} - F_i \int_0^h \frac{x_2 dx_2}{\nu + \nu_t} \right\}, \quad (B5)$$

where  $i = 1$  and  $3$ .  $\mu$  represents the dynamic viscosity of the fluid,  $h$  is the sampling height, and  $u_{hi}$  is the velocity at the sampling point in the LES domain.

The EQWM sets the source terms  $F_i$  to zero, such that Eq. (B5) can be simplified as follows:

$$\tau_{wi} = \mu \frac{\partial u_i}{\partial x_2} \Big|_{x_2=0} = \frac{\rho u_{hi}}{\int_0^h \frac{dx_2}{\nu + \nu_t}}. \quad (B6)$$

The EQWM only requires sampling the streamwise and spanwise velocity components at the sampling point. Since Eq. (B4) incorporates the law of the wall that accounts for near-wall velocity distribution, the EQWM is essentially equivalent to the ALG. The slight advantage of the former lies in its ability to produce correct wall shear stress even when the local grid approaches traditional LES resolution, i.e., when the viscous sublayer and buffer layer are well resolved.<sup>15</sup> However, further validation is still needed to assess the predictive performance of the EQWM in flows with strong adverse pressure gradients.

Due to the influence of adverse pressure gradients in separated flows, the NEQWM retains the pressure gradient term in the source terms. In such case,  $F_i$  can be expressed as

$$F_i = \frac{1}{\rho} \frac{\partial p}{\partial x_i}. \quad (B7)$$

Different from the EQWM, the NEQWM requires sampling the streamwise and spanwise velocity components as well as the pressure gradient at the sampling point.

REFERENCES

- <sup>1</sup>J. Smagorinsky, “General circulation experiments with the primitive equations: I. The basic experiment,” *Mon. Weather Rev.* **91**(3), 99–164 (1963).
- <sup>2</sup>E. R. Van Driest, “On turbulent flow near a wall,” *J. Aeronaut. Sci.* **23**(11), 1007–1011 (1956).
- <sup>3</sup>M. Germano, U. Piomelli, P. Moin, and W. H. Cabot, “A dynamic subgrid-scale eddy viscosity model,” *Phys. Fluids A* **3**(7), 1760–1765 (1991).
- <sup>4</sup>D. K. Lilly, “A proposed modification of the Germano subgrid-scale closure method,” *Phys. Fluids A* **4**(3), 633–635 (1992).
- <sup>5</sup>F. Nicoud and F. Ducros, “Subgrid-scale stress modelling based on the square of the velocity gradient tensor,” *Flow, Turbul. Combust.* **62**(3), 183–200 (1999).
- <sup>6</sup>A. Yoshizawa and K. Horiuti, “A statistically-derived subgrid-scale kinetic energy model for the large-eddy simulation of turbulent flows,” *J. Phys. Soc. Jpn.* **54**(8), 2834–2839 (1985).
- <sup>7</sup>W. W. Kim and S. Menon, “Application of the localized dynamic subgrid-scale model to turbulent wall-bounded flows,” AIAA Paper No. 97–0210, 1997.
- <sup>8</sup>U. Piomelli and E. Balaras, “Wall-layer models for large-eddy simulations,” *Annu. Rev. Fluid Mech.* **34**(1), 349–374 (2002).
- <sup>9</sup>D. R. Chapman, “Computational aerodynamics development and outlook,” *AIAA J.* **17**(12), 1293–1313 (1979).
- <sup>10</sup>H. Choi and P. Moin, “Grid-point requirements for large eddy simulation: Chapman’s estimates revisited,” *Phys. Fluids* **24**(1), 011702 (2012).
- <sup>11</sup>U. Schumann, “Subgrid scale model for finite difference simulations of turbulent flows in plane channels and annuli,” *J. Comput. Phys.* **18**(4), 376–404 (1975).
- <sup>12</sup>H. Werner and H. Wengle, “Large-eddy simulation of turbulent flow over and around a cube in a plate channel,” in *Turbulent Shear Flows 8*, edited by F. Durst, R. Friedrich, B. E. Launder, F. W. Schmidt, U. Schumann, and J. H. Whitelaw (Springer-Verlag Berlin, 1991), pp. 155–168.
- <sup>13</sup>D. B. Spalding, “A single formula for the law of the wall,” *J. Appl. Mech.* **28**(3), 455–458 (1961).

- <sup>14</sup>E. Balaras, C. Benocci, and U. Piomelli, “Two-layer approximate boundary conditions for large-eddy simulations,” *AIAA J.* **34**(6), 1111–1119 (1996).
- <sup>15</sup>J. Larsson, S. Kawai, J. Bodart, and I. Bermejo-Moreno, “Large eddy simulation with modeled wall-stress: Recent progress and future directions,” *Mech. Eng. Rev.* **3**(1), 15-00418 (2016).
- <sup>16</sup>T. Mukha, S. Rezaeiravesh, and M. Liefvendahl, “A library for wall-modeled large-eddy simulation based on OpenFOAM technology,” *Comput. Phys. Commun.* **239**, 204–224 (2019).
- <sup>17</sup>G. I. Park and P. Moin, “Space-time characteristics of wall-pressure and wall shear-stress fluctuations in wall-modeled large eddy simulation,” *Phys. Rev. Fluids* **1**(2), 024404 (2016).
- <sup>18</sup>L. M. Wang, R. F. Hu, and X. J. Zheng, “A comparative study on the large-scale-resolving capability of wall-modeled large-eddy simulation,” *Phys. Fluids* **32**(3), 035102 (2020).
- <sup>19</sup>W. W. Zhao, F. C. Zhou, G. Q. Fan, and D. C. Wan, “Assessment of subgrid-scale models in wall-modeled large-eddy simulations of turbulent channel flows,” *J. Hydrodyn.* **35**, 407–416 (2023).
- <sup>20</sup>M. Boxho, M. Rasquin, T. Toulorge, G. Dergham, G. Winkelmans, and K. Hillewaert, “Analysis of space-time correlations to support the development of wall-modeled LES,” *Flow, Turbul. Combust.* **109**(4), 1081–1109 (2022).
- <sup>21</sup>M. Skote and D. S. Henningson, “Direct numerical simulation of a separated turbulent boundary layer,” *J. Fluid Mech.* **471**, 107–136 (2002).
- <sup>22</sup>P. S. Iyer and M. R. Malik, “Wall-modeled large eddy simulation of flow over a wall-mounted hump,” AIAA Paper No. 2016–3186, 2016.
- <sup>23</sup>X. Ren, H. Su, H. H. Yu, and Z. Yan, “Wall-modeled large eddy simulation and detached eddy simulation of wall-mounted separated flow via OpenFOAM,” *Aerospace* **9**(12), 759 (2022).
- <sup>24</sup>C. Duprat, G. Balarac, O. Métais, P. M. Congedo, and O. Brugière, “A wall-layer model for large-eddy simulations of turbulent flows with/out pressure gradient,” *Phys. Fluids* **23**(1), 015101 (2011).
- <sup>25</sup>M. Wang and P. Moin, “Dynamic wall modeling for large-eddy simulation of complex turbulent flows,” *Phys. Fluids* **14**(7), 2043–2051 (2002).
- <sup>26</sup>S. T. Chen, L. C. Yang, W. W. Zhao, and D. C. Wan, “Wall-modeled large eddy simulation for the flows around an axisymmetric body of revolution,” *J. Hydrodyn.* **35**(2), 199–209 (2023).
- <sup>27</sup>P. Catalano, M. Wang, G. Iaccarino, and P. Moin, “Numerical simulation of the flow around a circular cylinder at high Reynolds numbers,” *Int. J. Heat Fluid Flow* **24**(4), 463–469 (2003).
- <sup>28</sup>L. M. Lourenco and C. Shih, “Characteristics of the plate turbulent near wake of a circular cylinder. A particle image velocimetry study,” unpublished results (1994).
- <sup>29</sup>C. Norberg, “An experimental investigation of the flow around a circular cylinder: Influence of aspect ratio,” *J. Fluid Mech.* **258**, 287–316 (1994).
- <sup>30</sup>L. Ong and J. Wallace, “The velocity field of the turbulent very near wake of a circular cylinder,” *Exp. Fluids* **20**(6), 441–453 (1996).
- <sup>31</sup>P. Parnaudeau, J. Carlier, D. Heitz, and E. Lamballais, “Experimental and numerical studies of the flow over a circular cylinder at Reynolds number 3900,” *Phys. Fluids* **20**(8), 085101 (2008).
- <sup>32</sup>P. Beaudan and P. Moin, “Numerical experiments on the flow past a circular cylinder at sub-critical Reynolds number,” NASA STI/Recon Technical Report No. TF-62, 1994.
- <sup>33</sup>M. Breuer, “Large eddy simulation of the subcritical flow past a circular cylinder: Numerical and modeling aspects,” *Int. J. Numer. Methods Fluids* **28**(9), 1281–1302 (1998).
- <sup>34</sup>A. G. Kravchenko and P. Moin, “Numerical studies of flow over a circular cylinder at  $Re_D = 3900$ ,” *Phys. Fluids* **12**(2), 403–417 (2000).
- <sup>35</sup>P. Sagaut, *Large Eddy Simulation for Incompressible Flows: An Introduction* (Springer Science & Business Media, 2005).
- <sup>36</sup>H. Jiang and L. Cheng, “Large-eddy simulation of flow past a circular cylinder for Reynolds numbers 400 to 3900,” *Phys. Fluids* **33**(3), 034119 (2021).
- <sup>37</sup>J. Franke and W. Frank, “Large eddy simulation of the flow past a circular cylinder at  $Re_D = 3900$ ,” *J. Wind Eng. Ind. Aerodyn.* **90**(10), 1191–1206 (2002).
- <sup>38</sup>H. Weller, “Controlling the computational modes of the arbitrarily structured C grid,” *Mon. Weather Rev.* **140**(10), 3220–3234 (2012).
- <sup>39</sup>J. Martínez, F. Piscaglia, A. Montorfano, A. Onorati, and S. M. Aithal, “Influence of spatial discretization schemes on accuracy of explicit LES: Canonical problems to engine-like geometries,” *Comput. Fluids* **117**, 62–78 (2015).
- <sup>40</sup>H. Jasak, “Error analysis and estimation for the finite volume method with applications to fluid flows,” Ph.D. thesis (Imperial College London, 1996).
- <sup>41</sup>X. Ma, G. S. Karamanos, and G. E. Karniadakis, “Dynamics and low-dimensionality of a turbulent near wake,” *J. Fluid Mech.* **410**, 29–65 (2000).
- <sup>42</sup>G. Tian and Z. Xiao, “New insight on large-eddy simulation of flow past a circular cylinder at subcritical Reynolds number 3900,” *AIP Adv.* **10**(8), 085321 (2020).
- <sup>43</sup>D. A. Lysenko, I. S. Ertesvåg, and K. E. Rian, “Large-eddy simulation of the flow over a circular cylinder at Reynolds number 3900 using the OpenFOAM toolbox,” *Flow, Turbul. Combust.* **89**(4), 491–518 (2012).
- <sup>44</sup>H. Ouvrard, B. Koobus, A. Dervieux, and M. V. Salvetti, “Classical and variational multiscale LES of the flow around a circular cylinder on unstructured grids,” *Comput. Fluids* **39**(7), 1083–1094 (2010).
- <sup>45</sup>H. Ali, N. B. Khan, M. Jameel, A. Khan, M. Sajid, A. Munir, A. E. S. Ahmed, K. A. M. Alharbi, and A. M. Galal, “Numerical investigation of the effect of spanwise length and mesh density on flow around cylinder at  $Re = 3900$  using LES model,” *PLoS One* **17**(4), e0266065 (2022).
- <sup>46</sup>N. B. Khan, Z. Ibrahim, A. B. Bin Mohamad Badry, M. Jameel, and M. F. Javed, “Numerical investigation of flow around cylinder at Reynolds number = 3900 with large eddy simulation technique: Effect of spanwise length and mesh resolution,” *Proc. Inst. Mech. Eng., Part M* **233**(2), 417–427 (2019).
- <sup>47</sup>Y. Jin, J. S. Cai, and F. Liao, “Comparative numerical studies of flow past a cylinder at Reynolds number 3900,” *Appl. Math. Mech.* **37**(12), 1282–1295 (2016).
- <sup>48</sup>C. Liu, Y. Gao, S. Tian, and X. Dong, “Rortex—A new vortex vector definition and vorticity tensor and vector decompositions,” *Phys. Fluids* **30**(3), 035103 (2018).
- <sup>49</sup>Y. Gao and C. Liu, “Rortex and comparison with eigenvalue-based vortex identification criteria,” *Phys. Fluids* **30**(8), 085107 (2018).
- <sup>50</sup>W. W. Zhao, J. H. Wang, and D. C. Wan, “Vortex identification methods in marine hydrodynamics,” *J. Hydrodyn.* **32**(2), 286–295 (2020).